ABSTRACT

Title of Thesis: TOWARDS HYBRID QUANTUM NETWORKING: INTERFACING ION TRAPS WITH NEUTRAL ATOM SYSTEMS

Brennan Romanoff
Masters of Science, 2025

Thesis Directed by: Dr. Qudsia Quraishi
Department of Physics

Building large-scale modular quantum computers and quantum networks require scalable high fidelity, high efficiency, and long lifetime quantum memories [1]. Quantum memories are proposed to increase photon-mediated matter-qubit entanglement rates by synchronizing photon interference between network nodes [2]. Hybrid quantum networking leverages trapped ions' high fidelity operations and neutral-atoms' single photon manipulation for increased entanglement rates over single-species quantum networks [3, 4, 5, 6, 7, 8]. Here, we aim to demonstrate flying-qubit photon storage in a neutral-atom system using frequency-converted photons entangled with a trapped barium ion. The quantum information encoded in the flying qubit's polarization states is reversibly mapped to a multiplexed dual-rail encoding scheme during storage. This work helps enable long-distance quantum networking by synthesizing hybrid components in entanglement distribution [9].

TOWARDS HYBRID QUANTUM NETWORKING: INTERFACING ION TRAPS WITH NEUTRAL ATOM SYSTEMS

by

Brennan James-Everett Romanoff

Thesis submitted to the Faculty of the Graduate School of the
University of Maryland, College Park in partial fulfillment
of the requirements for the degree of
Masters of Science
2025

Advisory Committee:
Dr. Qudsia S. Quraishi, Co-Chair/Advisor
Professor Nathan Schine, Co-Chair
Distinguished Chair Professor Saikat Guha

Dedication

To my Faith, Family, Professors, Mentors, and everyone who helped get me to where I am today.

Acknowledgments

First, I want to thank God for the opportunity to study what I love and blessing me with a wonderful family, friends, and colleagues. Secondly, I want to thank my wife, Ally (and our cats, DC and snips) for all the love and support throughout my program. Thirdly, I want to thank my parents, Danielle and Derek, my in laws, Amy and Kyle, and the rest of my family for loving and supporting me throughout my life. I would not be here today without any of them.

I would also want to thank my principal investigator, Qudsia Quraishi, and post-doctoral researcher, Kate Collins, for mentoring me during my time here at UMD and developing me into an experimentalist. I started with minimal knowledge and experience concerning my project, and now I am leaving two years later feeling like an expert in quantum memories. I could not have done this without the help of Qudsia and Kate.

Finally, I would like to thank my former professors and teachers who helped grow my love for understanding the natural world and mathematics.

Table of Contents

List of Figures

Chapter 1: Introduction

In the international year of quantum science and technology, the role of quantum information in changing the world cannot be understated. Alongside artificial intelligence (AI), quantum technology plays a significant role in the economy, national security, and even touches daily lives [10]. Numerous encryption protocols (e.g. Rivest-Shamir-Adleman (RSA), Elliptic curve discrete logarithm problem (ECDLP)) can be broken (i.e. can be solved in polynomial time in the number of quantum bits, or qubits for short, needed to describe the problem), by Shor's factorization algorithm which is a specific instance of the more general hidden sugroup problem (HSP). Generally, there exists quantum algorithms that can solve the general albelian HSP in polynomial time when classical algorithms require exponential. A potentially quantum-secure cryptosystem relies on the difficulty of solving the non-ableian HSP, despite only needing a polynomial number of queries [11]. Grover's quantum algorithm for unstructured search provides a quadratic speedup over classical computation for essentially finding a needle in a haystack. Beyond quantum computers, quantum sensing promises better global positioning systems (GPS), inertial sensors, radio frequency (RF) receivers, and technology sensing well below the standard quantum limit (SQL) [12]. The science devoted to understanding and developing the quantum science and technologies is known as **quantum information (QI)**. This thesis is devoted to better understand one technology and how it fits into the bigger picture of QI: quantum memories.

The thesis is organized into the following sections: chapter 1 is an introduction to quantum information, quantum networking, and hybrid systems; chapter 2 discusses the theory behind quantum memories and related experiments; chapter 3 covers the topics of

quantum memories and the state of the field; chapter 4 discusses the experimental setup; and chapter 5 is a summary and outlook for future projects.

1.1 Information Theory

The following section uses the treatment from Nielsen and Chuang's *Quantum Computation and Quantum Information* [13]. Information can be thought of as distinguishing between possible messages [14]. Classical information can be stored in bits of information, where each bit distinguishes between two messages: 0 and 1. Consequently, k bits can store up to 2^k possible messages. In the absence of noise, classical information can be measured and replicated without being altered.

Quantum information refers to the information stored in a quantum state. The quantum analog of a bit is a quantum bit, or qubit for short, that has a 2-dimensional vector space with orthonormal basis elements represented in the Dirac notation $|0\rangle$ and $|1\rangle$. A pure qubit state, $|\Psi\rangle$, can store any **superposition** of messages, 0 and 1 by

$$|\Psi\rangle = \alpha\,|0\rangle + \beta\,|1\rangle \tag{1.1}$$

for **probability amplitudes** $\alpha, \beta \in \mathbb{C}$ where the probability of measuring 0 is $Pr(0) = |\alpha|^2$, the probability of measuring 1 is $Pr(1) = |\beta|^2$, and $|\alpha|^2+|\beta|^2= 1$ is the normalization condition to ensure a valid probability distribution. Introducing the dual space notation $\langle\cdot|$, we can define the adjoint through an isomorphism

$$|\Phi\rangle = \gamma\,|0\rangle + \delta\,|1\rangle \Longleftrightarrow \langle\Phi| = \gamma^*\,\langle 0| + \delta^*\,\langle 1| \tag{1.2}$$

where * refers to the complex conjugate. Qubits live in **Hilbert space**, which is a complex vector space with an inner product defined by

$$\langle\Phi|\Psi\rangle = \alpha\gamma^*\,\langle 0|0\rangle + \beta\delta^*\,\langle 0|1\rangle \tag{1.3}$$

since $\langle m|n\rangle = \delta_{mn}$ where δ_{mn} is the Dirac delta defined as

$$\delta_{mn} = \begin{cases} 0 \text{ if } m \neq n \\ 1 \text{ if } m = n \end{cases}. \tag{1.4}$$

Furthermore, we can take the **tensor product** of two qubits

$$|a\rangle \otimes |b\rangle := |a\rangle\,|b\rangle = |a\ b\rangle \tag{1.5}$$

where the dimension of the combined Hilbert space is equal to the product of the dimension of the Hilbert space of each factor. Kets can be represented by column vectors and the tensor product is given as the tensor product of the column vectors.

Physical operations that preserve the quantum features of a qubit must preserve linearity and the inner product. The formalism for valid quantum operations uses **unitary operators** defined as $U : UU^\dagger = U^\dagger U = I$ where $\dagger$ represents the Hermitian adjoint (complex conjugate transpose). A unitary operator and it's Hermitian adjoint for a single qubit can be represented by 2×2 matrices

$$U = \begin{bmatrix} a & b \\ c & d \end{bmatrix} \text{ and } U^\dagger = \begin{bmatrix} a^* & c^* \\ b^* & d^* \end{bmatrix}. \tag{1.6}$$

where the rows and columns are orthonormal. Unitary matrices can be thought of as rotations since the modulus of the eigenvalue is always 1.

The following widely known No-Cloning Theorem provides a restriction on how quantum states can evolve.

Theorem 1.1.1. *There is no quantum operation that takes one copy of an arbitrary unknown quantum state and makes two copies.*

Proof. Consider the quantum states $|0\rangle, |1\rangle, \frac{1}{\sqrt{2}}[|0\rangle + |1\rangle]$ Suppose by way of contradiction (BWOC) that there exists a Unitary operator, U that takes as input a state $|a\rangle$ and ancilla

(i.e. auxillary) qubit $|0\rangle$ and outputs $|a\rangle\,|a\rangle$. Then,

$$U\,|0\rangle\,|0\rangle = |0\rangle\,|0\rangle \tag{1.7}$$

$$U\,|1\rangle\,|0\rangle = |1\rangle\,|1\rangle\,. \tag{1.8}$$

Since quantum mechanics is linear,

$$\begin{aligned} U\frac{1}{\sqrt{2}}[|0\rangle + |1\rangle]\,|0\rangle &= \frac{1}{\sqrt{2}}[U\,|0\rangle\,|0\rangle + U\,|1\rangle\,|0\rangle] \\ &= \frac{1}{\sqrt{2}}[|0\rangle\,|0\rangle + |1\rangle\,|1\rangle]. \end{aligned} \tag{1.9}$$

but by the definition of U,

$$\begin{aligned} U\frac{1}{\sqrt{2}}[|0\rangle + |1\rangle]\,|0\rangle &= \frac{1}{2}[|0\rangle + |1\rangle][|0\rangle + |1\rangle] \\ &= \frac{1}{2}[|0\rangle\,|0\rangle + |0\rangle\,|1\rangle + |1\rangle\,|0\rangle + |1\rangle\,|1\rangle]. \end{aligned} \tag{1.10}$$

Clearly, equations 1.10 and 1.9 are not equal, and the assumption that U exists is incorrect. Therefore, we conclude that no quantum operation that takes one copy of an arbitrary unknown quantum state and makes two copies. □

A striking feature of quantum information is **entanglement**. Entanglement has stronger than classical correlations and cannot be represented as a tensor product of two or more states. Furthermore, violations of the famous Bell inequality implies that entangled states cannot be simulated by local hidden variables [15]. The simplest case of entanglement is between two qubits

$$|\Psi\rangle = \frac{1}{\sqrt{2}}[|0\rangle\,|0\rangle + |1\rangle\,|1\rangle]. \tag{1.11}$$

Note that there is no way to decompose $|\Psi\rangle$ as a tensor product of two qubits. This can be seen by multiplying two arbitary qubit states

$$[\alpha\,|0\rangle + \beta\,|1\rangle] \otimes [\gamma\,|0\rangle + \delta\,|1\rangle] = \alpha\gamma\,|00\rangle + \alpha\delta\,|01\rangle + \beta\gamma\,|10\rangle + \beta\delta\,|11\rangle\,. \tag{1.12}$$

There is no $\alpha, \beta, \gamma, \delta \in \mathbb{C}$ that satisfies both $\alpha\gamma = \beta\delta = \frac{1}{\sqrt{2}}$ and $\alpha\delta = \beta\gamma = 0$. Therefore, this state is not the same as an equal probability mixture of each qubit being 0 or 1. Rather, that state is represented as

$$|\Phi\rangle = \frac{1}{2}[|00\rangle + |01\rangle + |10\rangle + |11\rangle]. \tag{1.13}$$

1.2 Quantum Networking

"Photonic interconnects between quantum processing nodes may be the only way to achieve large-scale quantum computers..." [1]

Despite recent progress in developing quantum computers, the largest quantum computer has over 1,000 physical qubits [16]. In the noisy intermediate-scale quantum era (NISQ), many physical qubits will be needed to encode a **logical bit**. The standard approach is to apply stabilizer codes where many physical qubits encode a bit, and errors can be corrected by measuring an error syndrome in an ancilla register [17]. Recent estimates of 600 physical bits may be needed to encode a logical qubit, but engineering a single quantum processor with millions of qubits remains a challenging feat [18].

Instead of scaling one processor with n qubits, the **distributed modular quantum computing** approach builds smaller quantum computers, each with n_i qubits satisfying $\sum_i n_i = n$, and connects them through **quantum networks** [1, 19]. Quantum networks enable the transmission of quantum states and distribution of entanglement across quantum information systems [10]. Furthermore, quantum networks enable an improved performance of multiple spatially distributed quantum sensors and quantum communications [20].

Quantum networks rely on excitations of the electromagnetic field, known as **pho-**

tons, to enable long-distance communication between remote network nodes [4]. In contrast to classical networks which can transmit classical information via amplification, quantum networks cannot copy quantum states per Thm. 1.1.1. Therefore, quantum networks must faithfully generate, store, and distribute entanglement [21].

One way to transmit quantum information is by writing the quantum state into the polarization of single photons at telecommunication wavelengths, and transmitting the photon over the network through fiber-optic infrastructure [22]; two other methods of writing a quantum state into a photon are time-bin and frequency-bin [1]. Due to fiber-optic loss being 0.2 dB/km, i.e. an exponential decrease in fidelity with distance, transmission without **quantum repeaters** is limited to approximately 100 km [23]. The range of a quantum network can be extended by decomposing a long fiber-optic link of length L into k smaller links connected by $k+1$ quantum repeaters with separation distance l_i between nodes i and $i+1$ satisfying $\sum_{i=1}^{k} l_i = L$. The maximum decrease in fidelity is now only $max_{\{l_i\}} 0.2 l_i$ dB for l_i measured in km [24]. Using a nested purification protocol, quantum repeaters may faithfully transmit signals over long distances [24]. Furthermore, repeaters require only polynomial overhead in time and a logarithmic overhead in the number of locally controlled particles [24].

A quantum repeater protocol requires heralded entanglement, storage in a **quantum memory**, and a swap operation [19]. Figure 1.1 exhibits the use of quantum repeaters in a quantum network to generate entanglement.

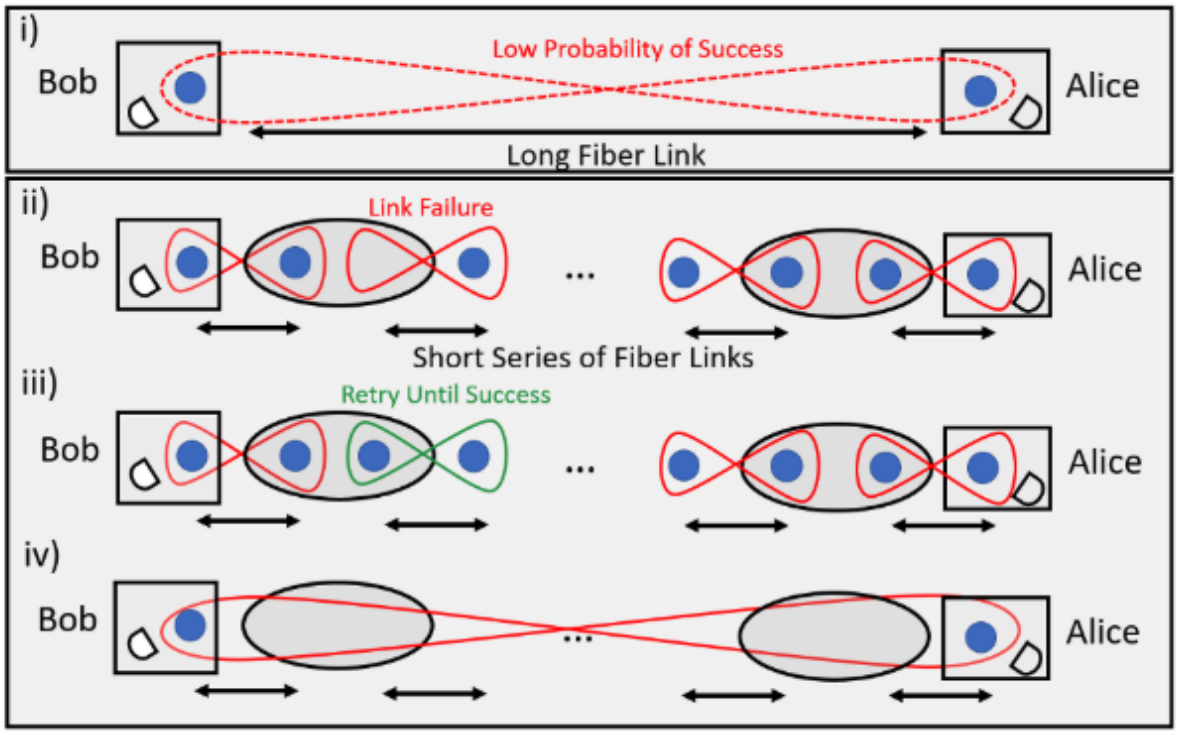

Figure 6: Quantum Repeaters and Quantum Networks. Quantum repeaters can extend the range of a quantum network by replacing a long fiber-optic link, where entangled photons are likely to be lost, with a series of shorter links. Each shorter link can attempt to distribute entanglement between repeaters multiple times, while successfully transmitted entanglement is stored in quantum memories. When entanglement is established on every link, the quantum repeaters can perform entanglement swaps to distribute it to the end users.

Figure 1.1: Quantum Network Conceptual Diagram taken from https://aws.amazon.com/blogs/quantum-computing/an-illustrated-introduction-to-quantum-networks-and-quantum-repeaters/

1.3 Hybrid Systems

Realizing quantum computers requires many qubits, high fidelity, and fault tolerance [25]. Hybrid quantum networking leverages the best attributes of different species for long-distance communication [2, 8, 9]. In this thesis, I will focus on exploiting trapped ions' high fidelity operations and neutral-atoms' single photon manipulation for increased entanglement rates over single-species quantum networks. Note that the following performance metrics are not necessarily realizable in one system simultaneously, but rather demonstrate optimal performance under specialized conditions.

1.3.1 Trapped Ions in Quantum Networks

Trapped-ion processors have several advantages compared to other qubits such as coherence times over an hour, 99.99916% single-qubit gate fidelity, 99.97% two-qubit gate fidelity, and 800 times lower logical rate than physical error rates [25, 26, 27]. Furthermore, ions have all-to-all connectivity, meaning that interactions are not excluded to nearest neighbors, and qubits can easily be measured mid-circuit and reinitialized [28]. The most significant obstacle facing trapped-ion processors is scaling the number of qubits [29]. Currently, no quantum computer based on trapped ions has over 100 physical qubits. Furthermore, the wavelengths typically used to address trapped ions are in the optical regime of the electromagnetic spectrum, which adds additional layers of complexity compared to qubits dealing with the RF part of the electromagnetic spectrum [27].

1.3.2 Neutral Atom Systems in Quantum Networks

Neutral atom systems are more scalable than ion traps, may require less overhead, have single-qubit gate fidelities of 99.96%, two-qubit gate fidelities of 99.7%, are dynamically reconfigurable, and excel at single photon manipulation [30, 31, 32, 33, 34, 35]. Since ion's struggle with scalability, the ability to interface with neutral atoms may prove mutually beneficial for quantum computing [9, 36].

Chapter 2: Theory

2.1 EIT

Electromagnetically induced transparency (EIT) may render an optically thick medium transparent, slow and even stop light [9, 37, 38]. The applications of the EIT interaction between light and matter are particularly attractive for QI and quantum networking since temporal synchronization is paramount to entanglement swapping, communications, metrology, and sensing [39]. EIT provides control over the light-matter interaction of so-called "dark state" coherent superpositions, where there is strong atom-light coupling due to collective enhancement [40].

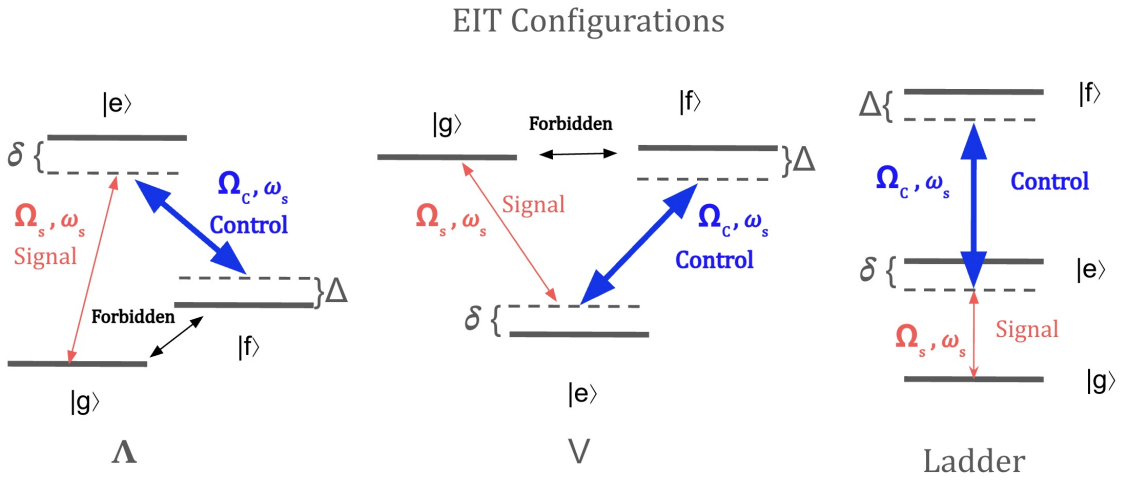

Figure 2.1: EIT Configurations. From left to right, Λ, V, and Ladder. Δ is the two-photon Raman detuning, δ is the detuning of the signal from resonance, and all other parameters are defined below

EIT serves as a storage mechanism for quantum memories by strongly coupling an

otherwise weak signal field to a long-lived excitation via another strong control laser sharing an intermediate state [41]. EIT can be performed in Λ, V, and ladder configurations as shown in figure 2.1, although V configurations do not offer much advtange for atomic systems [37, 42, 43]. The requirement for EIT is that there is a forbidden transition between states $|g\rangle$ and $|f\rangle$ where the signal field couples $|g\rangle$ with $|e\rangle$ and the strong control field couples $|f\rangle$ with $|e\rangle$. By strong, we mean the Rabi frequency of the control field is much greater than the all decoherence rates and decay rate of $|e\rangle$ to $|g\rangle$ or $|f\rangle$.

The following description of EIT uses a combination of the treatment from Wolfgang Ketterle's AMO 8.421 lecture notes and Irina Novikova's publication [41, 44]. The Hamiltonian in the rotating wave approximation for the system when both fields are on resonance (i.e. $\Delta = \delta = 0$) is

$$\hat{H}_{EIT} = \frac{\hbar\Omega_s}{2}(\hat{\sigma}_{eg}\hat{a}+\hat{\sigma}_{ge}\hat{a}^\dagger)+\frac{\hbar\Omega_c}{2}(\hat{\sigma}_{ef}\hat{c}+\hat{\sigma}_{fe}\hat{c}^\dagger)+\hbar\omega_s(\hat{a}^\dagger\hat{a}+\frac{1}{2})+\hbar\omega_c(\hat{c}^\dagger\hat{c}+\frac{1}{2})-\hbar\omega_{ef}\hat{\sigma}_{ff}-\hbar\omega_{eg}\hat{\sigma}_{gg} \tag{2.1}$$

where

$\hat{V} = \frac{\hbar\Omega_s}{2}(\hat{\sigma}_{eg}\hat{a} + \hat{\sigma}_{ge}\hat{a}^\dagger) + \frac{\hbar\Omega_c}{2}(\hat{\sigma}_{ef}\hat{c} + \hat{\sigma}_{fe}\hat{c}^\dagger)$ is the light-matter interaction energy,

$H_{light} = \hbar\omega_s(\hat{a}^\dagger\hat{a} + \frac{1}{2}) + \hbar\omega_c(\hat{c}^\dagger\hat{c} + \frac{1}{2})$ is the energy of the light fields,

$H_{atom} = -\hbar\omega_{ef}\hat{\sigma}_{ff} - \hbar\omega_{eg}\hat{\sigma}_{gg}$ is the atomic energy component,

$E_e := 0$ is the energy of state $|e\rangle$,

$E_g := -\hbar\omega_s$ is energy of the state $|g\rangle$,

$E_f := -\hbar\omega_c$ is energy of the state $|f\rangle$,

$\hat{a}$ is the annihilation operator between $|e\rangle$ and $|g\rangle$,

$\hat{c}$, is the annihilation operator between $|e\rangle$ and $|f\rangle$,

$\Omega_s := \langle e|\,\vec{\mu}\cdot\vec{E}\,|g\rangle\,/\hbar$ is the Rabi frequency coupling $|g\rangle$ to $|e\rangle$,

$\Omega_c := \langle e|\,\vec{\mu}\cdot\vec{E}\,|f\rangle\,/\hbar$ is the Rabi frequency coupling $|f\rangle$ to $|e\rangle$,

$\hat{\sigma_{ij}} := |i\rangle\langle j|$.

Diagonalizing the Hamiltonian, we find two eigenstates:

$$|B\rangle = \frac{\Omega_s}{\sqrt{\Omega_s^2 + \Omega_c^2}} |g\rangle + \frac{\Omega_c}{\sqrt{\Omega_s^2 + \Omega_c^2}} |f\rangle \tag{2.2}$$

$$|D\rangle = \frac{\Omega_c}{\sqrt{\Omega_s^2 + \Omega_c^2}} |g\rangle - \frac{\Omega_s}{\sqrt{\Omega_s^2 + \Omega_c^2}} |f\rangle . \tag{2.3}$$

Applying the light-matter interaction component of the Hamiltonian $\hat{V}|D\rangle$, we find

$$\begin{aligned} \hat{V}|D\rangle &= \frac{\hbar\Omega_s}{2}(\hat{\sigma}_{eg}\hat{a} + \hat{\sigma}_{ge}\hat{a}^\dagger)|D\rangle + \frac{\hbar\Omega_c}{2}(\hat{\sigma}_{ef}\hat{c} + \hat{\sigma}_{fe}\hat{c}^\dagger)|D\rangle \\ &= \frac{\hbar\Omega_s}{2}\hat{\sigma}_{eg}\hat{a}|D\rangle + \frac{\hbar\Omega_c}{2}\hat{\sigma}_{ef}\hat{c}|D\rangle \\ &= \frac{\hbar\Omega_s\Omega_c}{2\sqrt{\Omega_s^2 + \Omega_c^2}}|e\rangle - \frac{\hbar\Omega_c\Omega_s}{2\sqrt{\Omega_s^2 + \Omega_c^2}}|e\rangle \\ &= 0. \end{aligned} \tag{2.4}$$

The state $|D\rangle$ has a zero eigenvalue due to destructive interference between excitation pathways. Therefore, the $|D\rangle$ is decoupled from the state $|e\rangle$ under the light-matter interaction. Consequently, we call $|D\rangle$ the dark state and $|B\rangle$ the bright state (nonzero eigenvalue). When the fields are first applied, the atoms will be in some initial state and spontaneously emit. After some transient time, the system will evolve into the dark state and be stable against further illumination [44].

The previous description provides great insight into EIT, but the same result holds for nonzero detuning δ, albeit less insightful solutions [41, 44]. When $\Delta \neq 0$, the dark state precesses into the bright state by

$$|D_\delta(t)\rangle = \frac{\Omega_c}{\sqrt{\Omega_s^2 + \Omega_c^2}} |g\rangle - \frac{\Omega_s e^{i\Delta t}}{\sqrt{\Omega_s^2 + \Omega_c^2}} |f\rangle . \tag{2.5}$$

This provides an estimate of the dark state coherence time as $\tau_D \approx \frac{\pi}{2\Delta}$.

Conceptually, we may go into the dressed atom picture, we find a strong enough

control creates mixing between the excited state $|e\rangle$ and $|f\rangle$ to create new states $|e\rangle - |f\rangle$ and $|e\rangle + |f\rangle$. The signal mode Ω_s is tuned to $|e\rangle$ which is a dark resonance from destructive interference between the two excitation pathways to $|e\rangle - |f\rangle$ and $|e\rangle + |f\rangle$ as seen in figure 2.2.

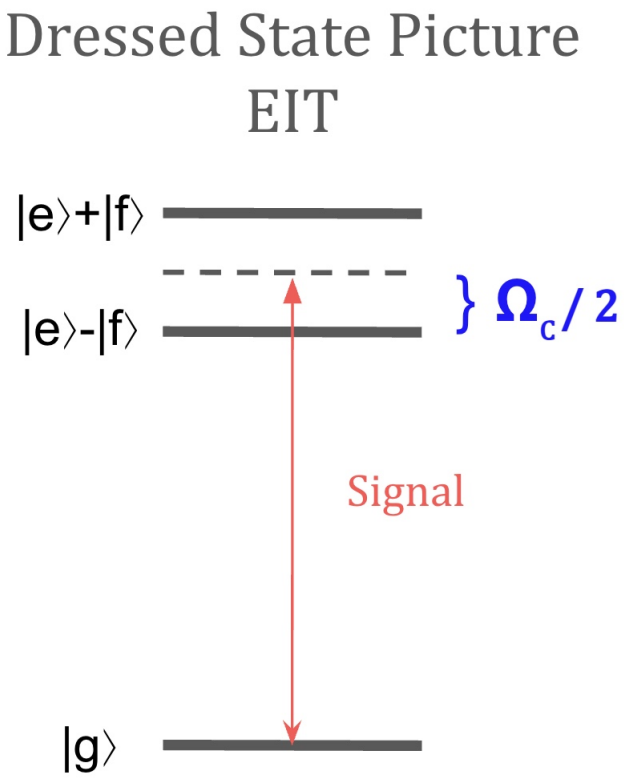

Figure 2.2: EIT in the Dressed State Picture.

Scanning the probe laser through the medium, there is a narrow peak for transmission on resonance when the control is on, where usually there is strong absorption. On resonance, the signal mode is coherently coupled to the dark state. Figure 2.3 displays the real and imaginary parts of the susceptibility compared in blue and red, respectively, compared to the absorption profile without EIT conditions (dashed black line).

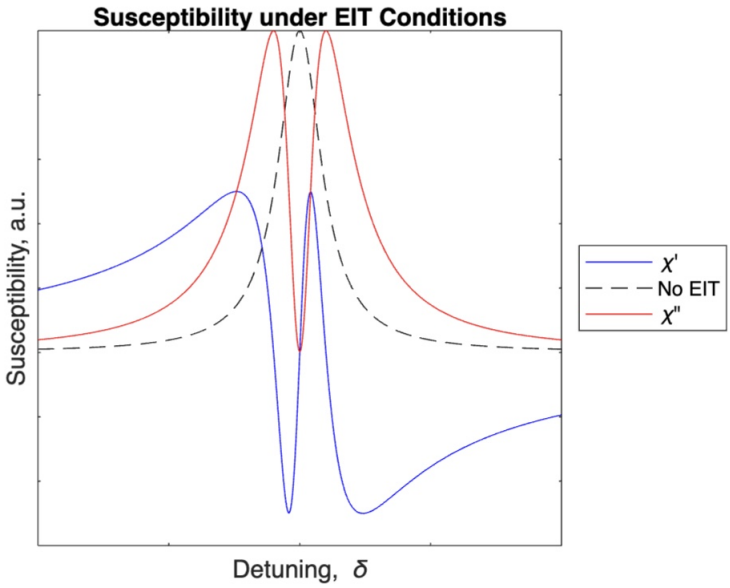

Figure 2.3: EIT Susceptibility.

2.1.1 Kramers-Kronig Relations

Since matter cannot respond instantaneously to an external perturbation, there exists a frequency dispersion of the index of refraction and a frequency-dependent response [45]. Consider a time-dependent conductivity $\sigma(\tau)$, in which we describe the response of matter to be *casual* (i.e. the current density depends on the field $t' < t$, but not $t' > t$). Furthermore, we assume that $\sigma(\tau) \to 0$ as $\tau \to \infty$ since events infinitely far away in time do not significantly affect the present. Therefore for a linear response,

$$\mathbf{j(r,}t) = \int_{-\infty}^{\infty} \sigma(t - t')\mathbf{E(r,}t)dt' \tag{2.6}$$

where the conductivity amplitude time dependence incorporates causality. We define the Fourier transform pair

$$\sigma(t) = \int_{-\infty}^{\infty} \hat{\sigma}(\omega)e^{-i\omega t}d\omega \tag{2.7}$$

$$\hat{\sigma}(\omega) = \frac{1}{2\pi}\int_{-\infty}^{\infty} \sigma(t)e^{i\omega t} \tag{2.8}$$

Therefore,

$$\hat{j}(\omega) = \hat{\sigma}(\omega)\hat{E}(\omega). \tag{2.9}$$

Since **j(r,**t) and **E(r,**t) are both real, σ must also be real (i.e. $\sigma(\tau) = \sigma^*(\tau)$). Splitting $\sigma(\omega)$ into real and imaginary components, $\sigma'(\omega)$ and $\sigma''(\omega)$, respectively, and combining this fact with equation 2.7,

$$\sigma(t) = \int_{-\infty}^{\infty} \hat{\sigma}(\omega)e^{-i\omega t}d\omega = \int_{-\infty}^{\infty} \hat{\sigma^*}(\omega)e^{i\omega t}d\omega = \sigma^*(t) \tag{2.10}$$

$$\implies \int_{-\infty}^{\infty} (\sigma'(\omega) + i\sigma''(\omega))e^{-i\omega t}d\omega = \int_{-\infty}^{\infty} (\sigma'(\omega) - i\sigma''(\omega))e^{i\omega t}d\omega \tag{2.11}$$

$$\implies \int_{-\infty}^{\infty} (\sigma'(-\omega) + i\sigma''(-\omega))e^{i\omega t}d\omega = \int_{-\infty}^{\infty} (\sigma'(\omega) - i\sigma''(\omega))e^{i\omega t}d\omega \tag{2.12}$$

$$\implies \sigma'(-\omega) = \sigma'(\omega) \text{ and } \sigma''(-\omega) = -\sigma''(\omega). \tag{2.13}$$

The electric susceptibility is similarly defined by

$$\hat{P}(r,\omega) = \epsilon_0\hat{\chi}(w)\hat{E}(r,w). \tag{2.14}$$

Likewise,

$$\chi'(-\omega) = \chi'(\omega) \text{ and } \chi''(-\omega) = -\chi''(\omega). \tag{2.15}$$

Imposing causality, we can arrive at the Kramer's Kronig relations which tell us that there exists a relationship between the real and imaginary parts of the susceptibility:

$$\chi'(\omega) = \frac{-1}{\pi}P\int_{-\infty}^{\infty} \frac{\chi''}{\omega - s}ds \tag{2.16}$$

$$\chi''(\omega) = \frac{1}{\pi}P\int_{-\infty}^{\infty} \frac{\chi'}{\omega - s}ds \tag{2.17}$$

where P stands for the principal value [45].

Furthermore, the imaginary part of the susceptibility is related to the absorption and the real part is related to the dispersion [40].

2.1.2 Slow Light

One can calculate the susceptibility for EIT (see [41]) under typical approximations to find the absorption and dispersion curves (see fig. 2.3). The group velocity is determined by the slope of the imaginary part of the susceptibility, which is maximum for EIT at $\delta = 0$. In general, the group velocity is given by

$$v_g = \frac{c}{n_g(\omega)} = \frac{c}{n + \omega_s \frac{dn}{d\omega_s}} \tag{2.18}$$

where n_g is the refractive index given by $n_g = 1 + \chi'$. Assuming $\delta << \Omega_c, \gamma_{ge}$ where γ_{ge} is the decay rate between $|e\rangle$ and $|g\rangle$, the group velocity of the probe is

$$v_g = \frac{c}{1 + \frac{c\alpha_0}{\pi\gamma_{ge}} \frac{|\Omega_c|^2}{\gamma_{EIT}^2}} \tag{2.19}$$

where α_0 is the unsaturated resonant absorption coefficient defined to be

$$\alpha_0 = \frac{k_p}{2\chi_p(0)} = \frac{k_p N \mu_{ge}^2}{2\hbar\epsilon_0\gamma_{ge}} \tag{2.20}$$

where $k_p = \frac{\omega_s}{c}$ and N is the number of atoms per unit volume. γ_{EIT} is the EIT linewidth given by

$$\gamma_{EIT} = \gamma_{gf} + \frac{|\Omega_c|^2}{\gamma_{ge}} \tag{2.21}$$

where γ_{gf} is the decay rate between states $|g\rangle$ and $|f\rangle$ [41].

Therefore, the group velocity in equation 2.19 can be dynamically controlled by changing Ω_c. In lab, this corresponds to changing the optical power, shape, and phase of the control field.

2.1.3 Stopped Light

During EIT, the state is

$$\sum_n e^{i\Delta k x_n} \hat{a}^{\dagger(n)} |0\rangle^{\otimes n} \tag{2.22}$$

where $\Delta k = \omega_s/c - \omega_c/c$ [46]. Since we do not know which atom absorbs the photon during EIT and each atom has a phase proportional to the phase of the difference in wavevectors, we call this a "spin-wave." Defining a mixing angle θ given by

$$c \cdot cos^2\theta = n_g(t) \tag{2.23}$$

we can switch between the photonic character and spin-wave character. In the limit that $|\Omega_c|^2 \to \infty$ (i.e. strong drive field), $\theta \to 0$, we have purely photonic character with $n_g \to c$ [40]. In the opposite limit as $|\Omega_c|^2 \to 0$, $\theta \to \frac{\pi}{2}$ and the signal field is mapped to a purely spin-wave character of the dark state coherence [40]. The mixing of θ be seen in figure 2.4 and the corresponding light and spin-wave dynamics can be seen in figure 2.5. The blue is the evolution of the light-component and the green is the evolution of the spin-wave component over storage. The time evolution can be seen in figure 2.6.

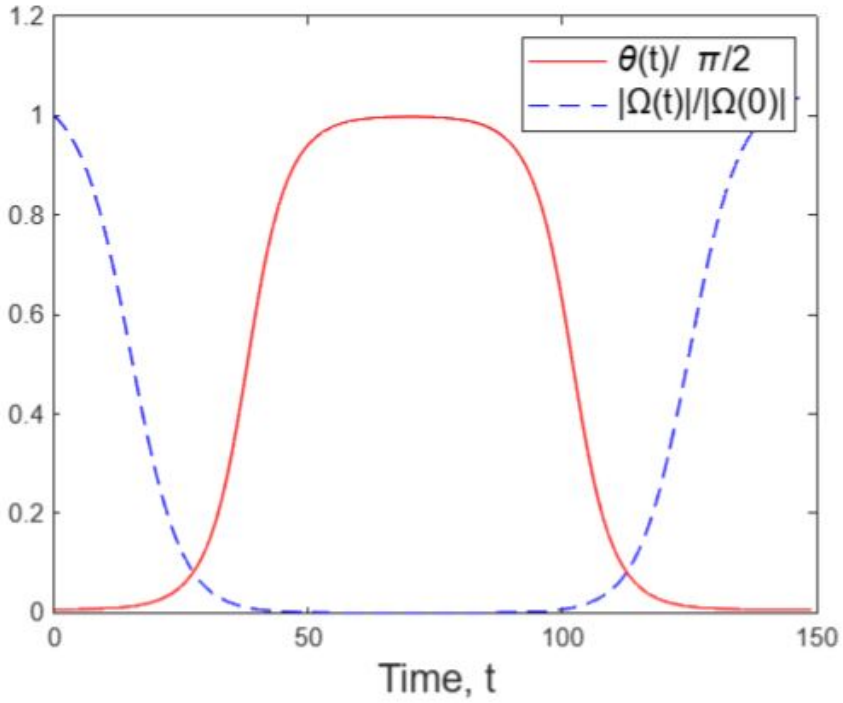

Figure 2.4: Mixing Angle

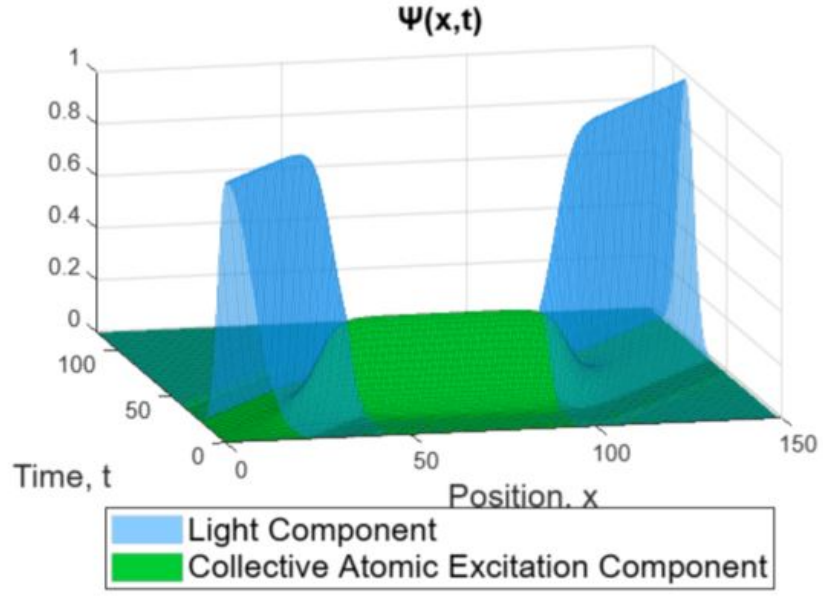

Figure 2.5: Light and Spin-Wave Dynamics in EIT

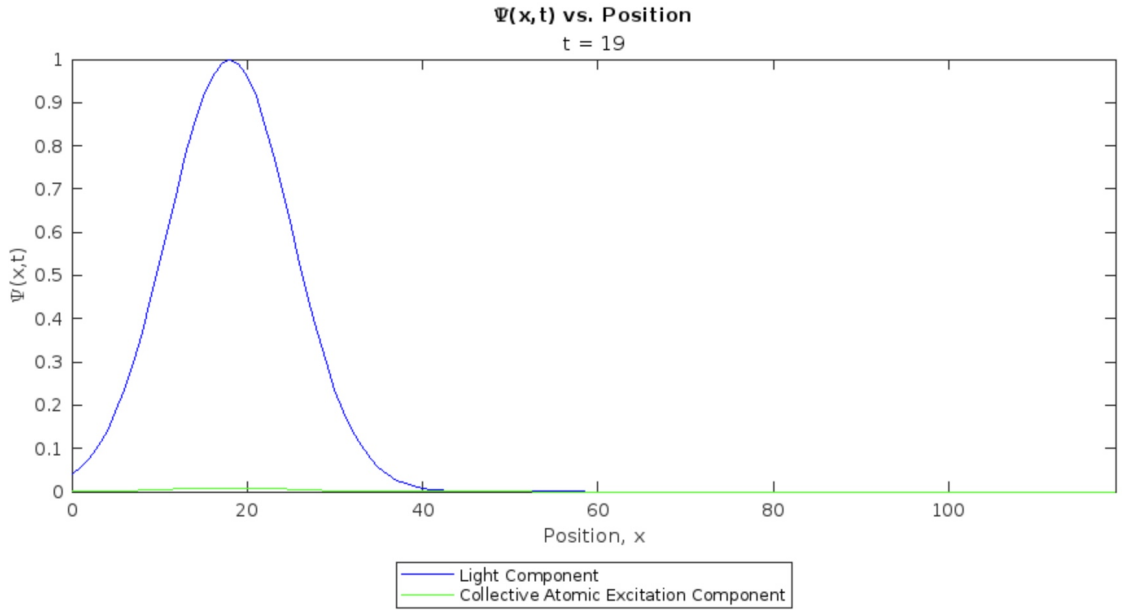
Ψ(x,t) vs. Position
t = 19
Ψ(x,t)
Position, x
Light Component
Collective Atomic Excitation Component

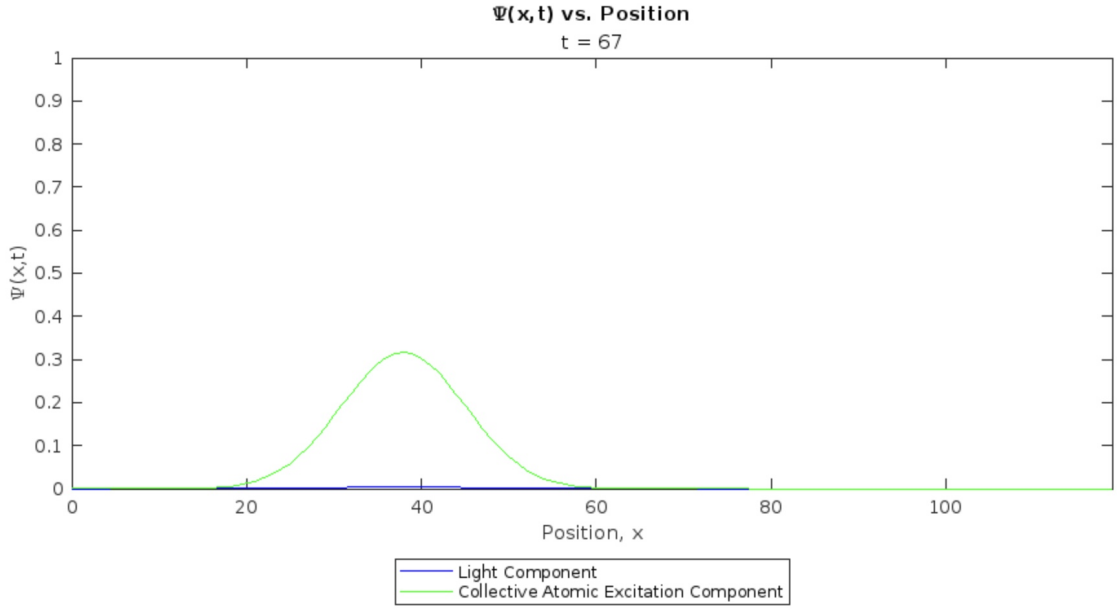
Ψ(x,t) vs. Position
t = 67
Ψ(x,t)
Position, x
Light Component
Collective Atomic Excitation Component

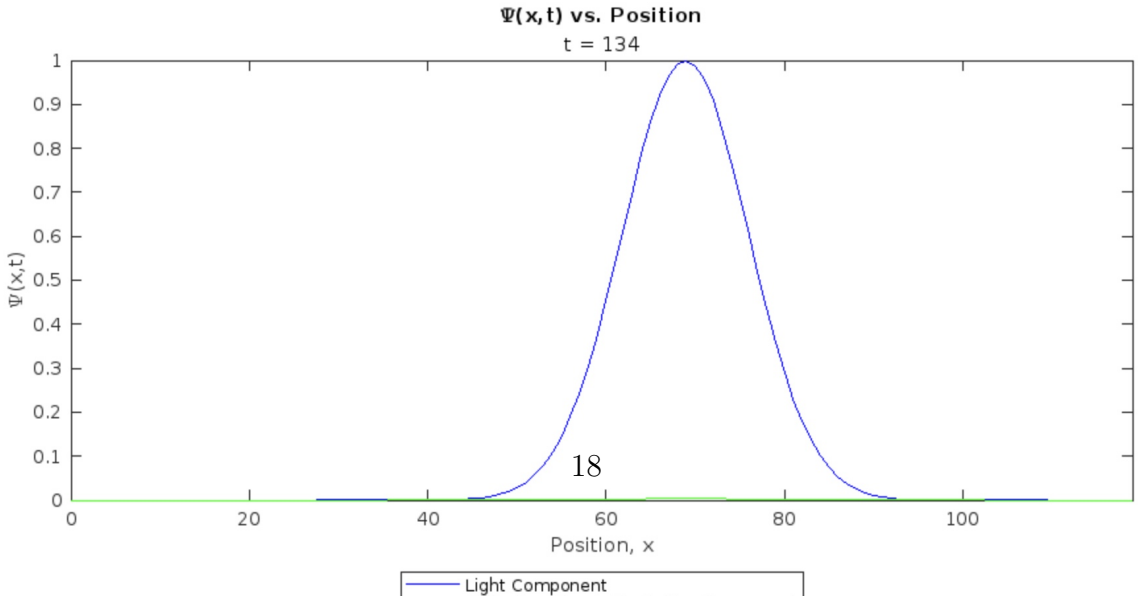
Ψ(x,t) vs. Position
t = 134
Ψ(x,t)
Position, x
Light Component

Therefore, we can reversibly map the photonic component $\hat{\mathcal{E}}(z)$ to the spin-wave component $\sigma_{fg}e^{i\Delta k(z+\int_0^\infty d\tau c\cdot cos^2(\theta(\tau)))}$ [40]

$$\hat{\mathcal{E}}(z) \Leftrightarrow \sigma_{fg}e^{i\Delta k(z+\int_0^\infty d\tau c\cdot cos^2(\theta(\tau)))}. \tag{2.24}$$

2.2 Entanglement Swapping

Distributing entanglement over long distances requires quantum repeaters at network nodes to swap entanglement at elementary links [19, 23, 24]. The optimal architecture to achieve the highest entanglement swapping rates in quantum networks is generating entanglement between some species and photons in independent registers, storing entangled photons in quantum memories, and swapping entanglement via a Bell-state measurement (BSM) [47, 48]. To herald entanglement, the photons must be indistinguishable in all the crucial degrees of freedom e.g. temporally, spectrally, when they interfere at the BSM [49]. A Hong-Ou-Mandel (HOM) interference measurement provides a method to verify the indistinguishability of single photons.

2.2.1 Hong-Ou-Mandel Interference

The following section is a generalization from a problem set in Dr. Nathan Schine's AMO course. Consider a non-polarizing beamsplitter (BS) with a single-photon state input to each port. Then with probability T, each photon is transmitted and with probability R=1-T, each photon is reflected. Figure 2.7 shows two input modes in ports 1 and 2 and their corresponding output modes in ports 3 and 4. For clarity, the beams are not overlapping in figure 2.7, but in reality, both photons must overlap in space and direction.

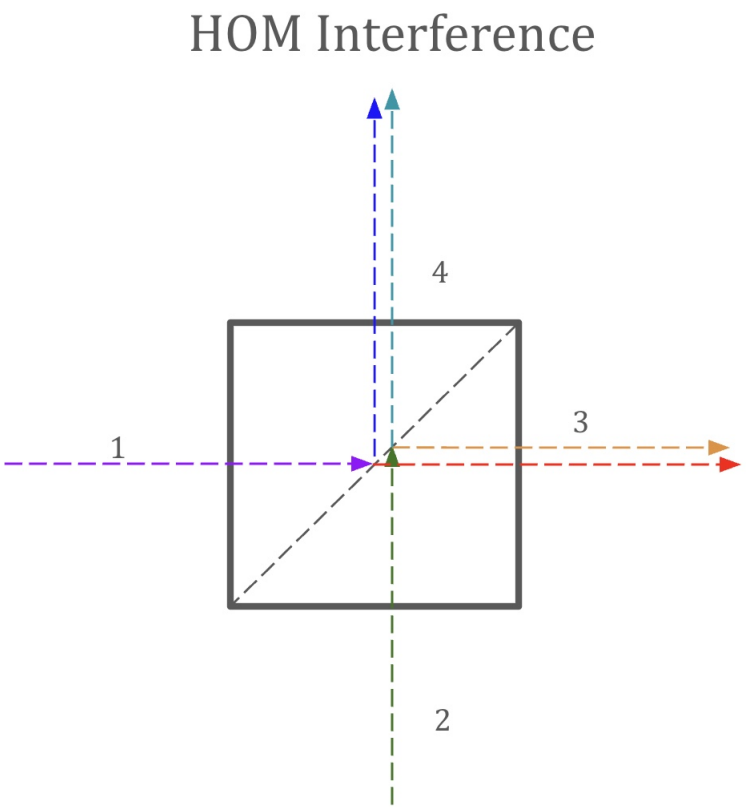

Figure 2.7: HOM Interference.

Using treatment from quantum optics, the BS unitary can be represented by the unitary matrix

$$\begin{bmatrix} \hat{a}_3 \\ \hat{a}_4 \end{bmatrix} = \begin{bmatrix} \sqrt{T} & e^{i\phi}\sqrt{R} \\ -e^{-i\phi}\sqrt{R} & \sqrt{T} \end{bmatrix} \begin{bmatrix} \hat{a}_1 \\ \hat{a}_2 \end{bmatrix} \tag{2.25}$$

where ϕ is the phase shift [50].

Assuming n_1 photons in port 1 and n_2 photons in port 2, the cross correlations are

$$\langle n_1 n_2 | \, \hat{n}_3 \hat{n}_4 \, | n_1 n_2 \rangle = \langle n_1 n_2 | \, \hat{a}_3^\dagger \hat{a}_3 \hat{a}_4^\dagger \hat{a}_4 \, | n_1 n_2 \rangle \, . \tag{2.26}$$

Substituting equation 2.25, the cross correlations are

$$\langle n_1 n_2| \, (\sqrt{T}\hat{a}_1^\dagger - e^{i\phi}\sqrt{R}\hat{a}_2^\dagger)(\sqrt{T}\hat{a} + e^{i\phi}\sqrt{R}\hat{a}_2)(e^{-i\phi}\sqrt{R}\hat{a}_1 + \sqrt{T}\hat{a}_2)(-e^{-i\phi}\sqrt{R}\hat{a}_1 + \sqrt{T}\hat{a}_2) \, |n_1 n_2\rangle \, . \tag{2.27}$$

Using a 50:50 (T:R) BS, $\phi = 0$, and one photon in each mode, many of the cross terms in equation 2.27 cancel and we are left with

$$\begin{aligned} \langle 1_1 1_2| \, \hat{n}_3 \hat{n}_4 \, |1_1 1_2\rangle = \frac{1}{4}(&\langle 1_1 1_2| \, \hat{n}_1 \hat{n}_1 \, |1_1 1_2\rangle + \langle 1_1 1_2| \, \hat{n}_1 \hat{n}_2 \, |1_1 1_2\rangle \\ &- \langle 1_1 1_2| \, (\hat{n}_1 + 1)\hat{n}_2 \, |1_1 1_2\rangle \\ &- \langle 1_1 1_2| \, (\hat{n}_2 + 1)\hat{n}_1 \, |1_1 1_2\rangle \\ &+ \langle 1_1 1_2| \, \hat{n}_1 \hat{n}_2 \, |1_1 1_2\rangle + \langle 1_1 1_2| \, \hat{n}_2 \hat{n}_1 \, |1_1 1_2\rangle) \end{aligned} \tag{2.28}$$

which simplifies to

$$\langle 1_1 1_2| \, (n_1(n_1 - 1) + n_2(n_2 - 1)) \, |1_1 1_2\rangle = 0. \tag{2.29}$$

We conclude there can never be one photon at port 3 and port 4 simultaneously if there are two indistinguishable photons entering ports 1 and port 2 of a 50:50 BS at the same time.

2.2.2 Single Photon $g^{(2)}$ Measurement

A $g^{(2)}$ measurement is an intensity correlation given by

$$g^{(2)}(\vec{r_1}, \vec{r_2}, t, \tau) = \frac{< \hat{E}^-(\vec{r_1}, t)\hat{E}^-(r_2, \vec{t} + \tau)\hat{E}^+(r_2, \vec{t} + \tau)\hat{E}^+(\vec{r_1}, t) >}{< \hat{E}^-(r_2, \vec{t} + \tau)\hat{E}^+(r_2, \vec{t} + \tau) >< \hat{E}^-(\vec{r_1}, t)\hat{E}^+(r_1, \vec{t}) >} \tag{2.30}$$

where $< \cdot >$ indicates a time average over t and τ is the relative delay between times when the operators are measured.

For a single photon entering port 1 and vacuum injected into port 2 of a 50:50 BS, $g^{(2)}$ becomes

$$g^{(2)}(\tau) = \frac{< \hat{a}_3^\dagger(t)\hat{a}_4^\dagger(t+\tau)\hat{a}_4(t+\tau)\hat{a}_3(t) >}{< \hat{a}_4^\dagger(t+\tau)\hat{a}_4(t+\tau) >< \hat{a}_3^\dagger(t) > \hat{a}_3(t)}. \tag{2.31}$$

Using equation 2.25, we find that equation 2.31 is the same as

$$g^{(2)}(\tau) = \frac{< \hat{a}_1^\dagger(t)\hat{a}_1^\dagger(t+\tau)\hat{a}_1(t+\tau)\hat{a}_1(t) >}{< \hat{a}_1^\dagger(t+\tau)\hat{a}_1(t+\tau) >< \hat{a}_1^\dagger(t) > \hat{a}_1(t)} = \frac{< \hat{n}_1(\hat{n}_1 - 1) >}{< \hat{n}_1^2 >}. \tag{2.32}$$

Therefore, for single photons, $g^{(2)}(0) = 0$. Experimentally, this can be realized by sending single photons into an input port of a BS and monitoring the output ports with photodetectors as in figure 2.8.

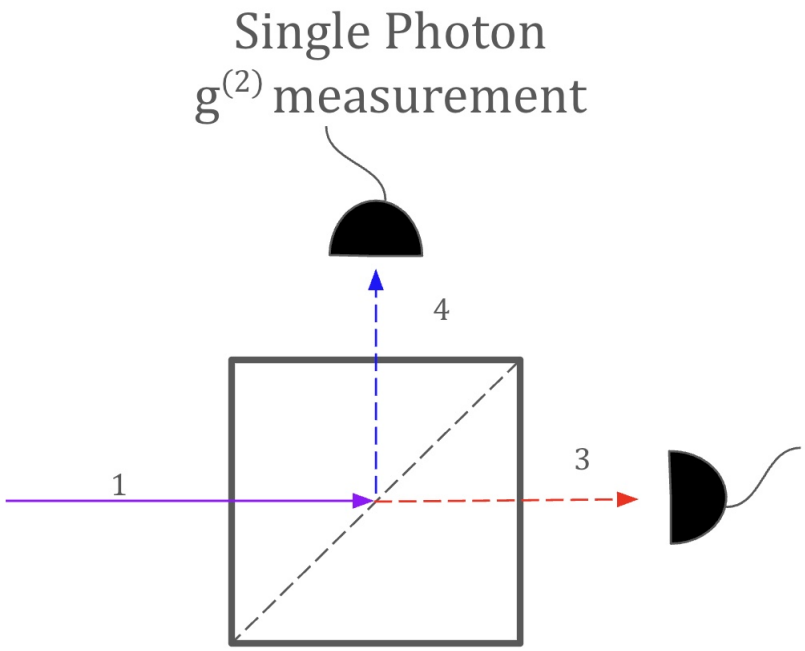

Figure 2.8: Single Photon $g^{(2)}$ Experimental Setup.

2.2.3 Bell State Measurement (BSM)

The four Bell states are defined as

$$\left|\Phi^{\pm}\right\rangle := \frac{1}{\sqrt{2}}(|00\rangle \pm |11\rangle) \tag{2.33}$$

and

$$\left|\Psi^{\pm}\right\rangle := \frac{1}{\sqrt{2}}(|01\rangle \pm |10\rangle). \tag{2.34}$$

A bell state measurement is an entangled projective measurement Π_{xz} on two qubits with two classical bits xz as the outcome

$$\Pi_{00} = \left|\Phi^{+}\right\rangle \left\langle\Phi^{+}\right| \tag{2.35}$$

$$\Pi_{01} = \left|\Phi^{-}\right\rangle \left\langle\Phi^{-}\right| \tag{2.36}$$

$$\Pi_{10} = \left|\Psi^{+}\right\rangle \left\langle\Psi^{+}\right| \tag{2.37}$$

$$\Pi_{11} = \left|\Psi^{-}\right\rangle \left\langle\Psi^{-}\right|. \tag{2.38}$$

The Bell measurement can be implemented by performing a controlled-NOT gate with the control on qubit 2 and target on qubit 1 followed by a Hadamard on qubit 2. The matrix representations are

$$cNOT := \begin{bmatrix} 1 & 0 & 0 & 0 \\ 0 & 1 & 0 & 0 \\ 0 & 0 & 0 & 1 \\ 0 & 0 & 1 & 0 \end{bmatrix} \tag{2.39}$$

and

$$H := \frac{1}{\sqrt{2}} \begin{bmatrix} 1 & 1 \\ 1 & -1 \end{bmatrix}. \tag{2.40}$$

2.2.4 BSM for Entanglement Swapping

Consider two $|\Phi^+\rangle$ Bell states

$$[\frac{1}{\sqrt{2}}(|00\rangle + |11\rangle)]^{\otimes 2} \tag{2.41}$$

Performing a BSM on qubits 2 and 3, the resulting state is

$$\begin{aligned} H_2 CNOT_{23} \frac{1}{2}(|0000\rangle + |1100\rangle + |0011\rangle + |1111\rangle) &= \frac{1}{2} H_2(|0000\rangle + |1110\rangle + |0011\rangle + |1101\rangle) \\ &= \frac{1}{2\sqrt{2}}(|0000\rangle + |0100\rangle + |1010\rangle - |1110\rangle \\ &\quad + |0011\rangle + |0111\rangle + |1001\rangle - |1101\rangle\,. \end{aligned} \tag{2.42}$$

Measuring the 2nd and 3rd qubits, if we measure xz and discard the 2nd and 3rd qubit, the state becomes

$$00 \rightarrow \left|\Phi^+\right\rangle \tag{2.43}$$

$$01 \rightarrow \left|\Psi^+\right\rangle \tag{2.44}$$

$$10 \rightarrow \left|\Phi^-\right\rangle \tag{2.45}$$

$$11 \rightarrow \left|\Psi^-\right\rangle. \tag{2.46}$$

Experimentally, we can overlap two photons that are each entangled with another species on a PBS as shown in figure 2.9 with unnormalized states.

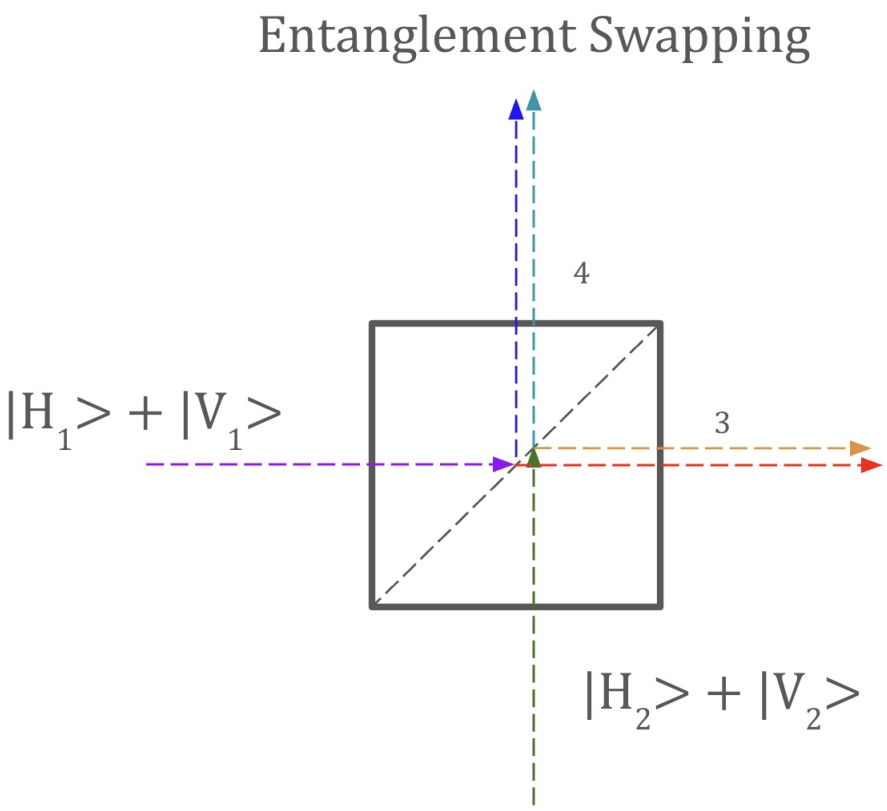

Figure 2.9: Entanglement Swapping using a PBS.

If both photons are indistinguishable, we measure one the following possibilities at port 3:

$$|V_2\rangle, |H_1\rangle, |0\rangle, |H_1V_2\rangle \tag{2.47}$$

with the correlated results at port 4:

$$|V_1\rangle, |H_2\rangle, |V_1H_2\rangle, |0\rangle. \tag{2.48}$$

WLOG, we can represent the global state prior to the PBS as

$$(|0_1H_10_2H_2\rangle + |0_1H_11_2V_2\rangle + |1_1V_10_2H_2\rangle + |1_1V_11_2V_2\rangle) \tag{2.49}$$

If we measure a single photon at port 3 (correspondingly we would measure single photon at port 4, the global state is projected into

$$\frac{1}{\sqrt{2}}(|0_1 0_2\rangle + |1_1 1_2\rangle) \tag{2.50}$$

which is found by summing over the combinations in equations 2.47 and 2.48. If we measure two photons at port 3, the state is projected into

$$|0_1 1_2\rangle \tag{2.51}$$

and likewise for two photons at port 4, the state is projected into

$$|1_1 0_2\rangle\,. \tag{2.52}$$

With this basic setup, we herald entanglement 50% of the time, known deterministically if we have nonzero cross correlations at the two ports.

Chapter 3: Quantum Memories

3.1 Overview

Quantum memories that can faithfully and efficiently preserve quantum information and deterministically transmit at a later time are critical to realizing quantum networks [51]. Due to the quantum nature of photons, the most practical implementation will be realized by sending photons through optical fiber links [23]. The basic idea of a quantum memory illustrated in figure 3.1: a signal field carrying quantum information is stored in some quantum memory media with the help of some control field. After a deterministic storage duration, the signal can be retrieved for further use (e.g. BSM entanglement swapping).

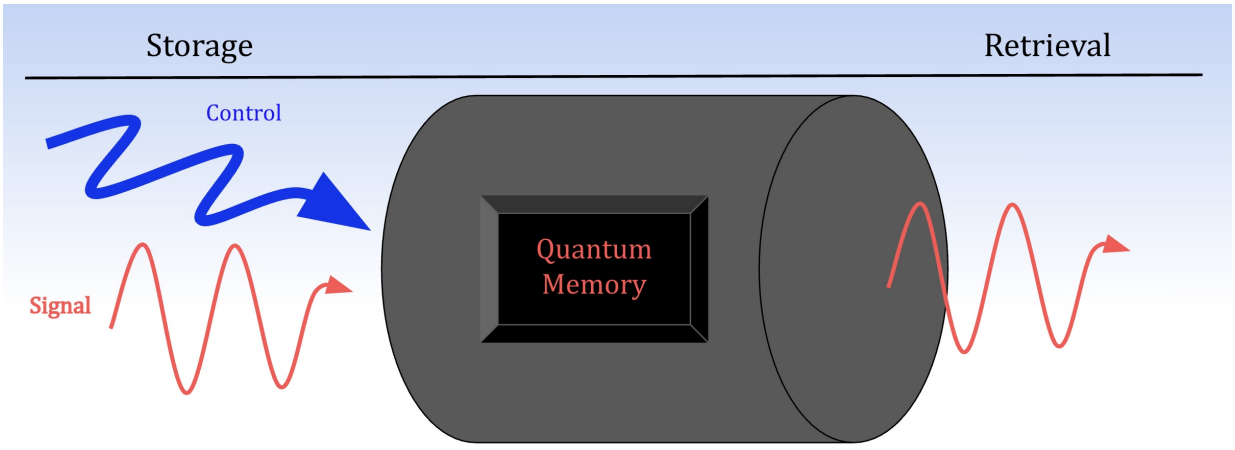

Figure 3.1: Elementary Quantum Memory.

Quantum memories can be used to synchronize operations in linear quantum computing [52], enable teleportation-based quantum repeaters for long-distance quantum communications beyond the loss limitation in optical fibers [24], obtain precision quantum measurements based on the quantum interference of atomic ensembles and thereby improve the precision of magnetometry, atomic clocks and spectroscopy [53],and as a cache memory [54].

Recent advances in the field have quantum memory efficiencies greater than 90 percent in magneto optical traps and 67 percent in warm atomic vapors. Fidelities above 95 percent have been recorded in multiple experiments. In warm atomic vapors, lifetimes have been reported on the order of hundreds of milliseconds.

Vapor cells are particiularly appealing to develop scalable photonic quantum repeaters.

3.2 Metrics

Retrieved flying qubits must output a state as close to the input as possible, store memory for as long as possible, and not have significant photon loss. These conditions are quantified respectively by fidelity, storage duration, and efficiency.

3.2.1 Efficiency

The efficiency of the quantum memory is defined for **unnormalized** $|\Psi_{in}\rangle$, $|\Psi_{out}\rangle$

$$\eta = \frac{\int |\Psi_{out,unnormalized}(\tau)|^2 d\tau}{\int |\Psi_{in,unnormalized}(\tau)|^2 d\tau} \tag{3.1}$$

Experimentally, this is the ratio of the optical power of the signal field prior to the quantum memory storage versus after retrieval.

3.2.2 Fidelity

The fidelity of an arbitrary quantum state after storage can be written as the overlap with the ideal state.

$$F = |\langle \Psi_{in} | \Psi_{out} \rangle|^2 \tag{3.2}$$

with **normalized** $|\Psi_{in}\rangle$ and $|\Psi_{out}\rangle$. We can perform state tomography after the quantum memory by initializing $\left|\Psi_{in}^{H}\right\rangle := |H\rangle), \left|\Psi_{in}^{V}\right\rangle := |V\rangle), \left|\Psi_{in}^{D}\right\rangle := |D\rangle) = \frac{1}{2}(|H\rangle + |V\rangle)$, and $\left|\Psi_{in}^{L}\right\rangle := |L\rangle) = \frac{1}{2}(|H\rangle + i\,|V\rangle)$. Experimentally, we can use a half-wave plate (HWP), quarter-wave plate (QWP), and polarizing beam splitter (PBS) to measure the fidelity. We cycle the HWP for a fixed QWP position to measure statistics in the transmitted and reflected paths of the PBS. The QWP allows us to vary the relative phase of the superposition while the HWP allows us to vary the relative amplitude.

3.2.3 Storage Duration

The storage duration is predetermined by the user in EIT [38]. Due to decoherence, the storage duration will be upper bounded by the minimum of the T_1 and T_2 times where T_1 time is the spin-relaxation time to the ground state and T_2 is the decoherence time.

3.3 Quantum Memory Media

Quantum memories have been realized in warm atoms, cold atoms, ion-doped solids, color centers, and solid-state systems [21, 37, 51, 55, 56, 57, 58, 59, 60]. Figures 3.2 and 3.3 below are experimental setups for color centers and ion-doped crystals, respectively [59, 60]:

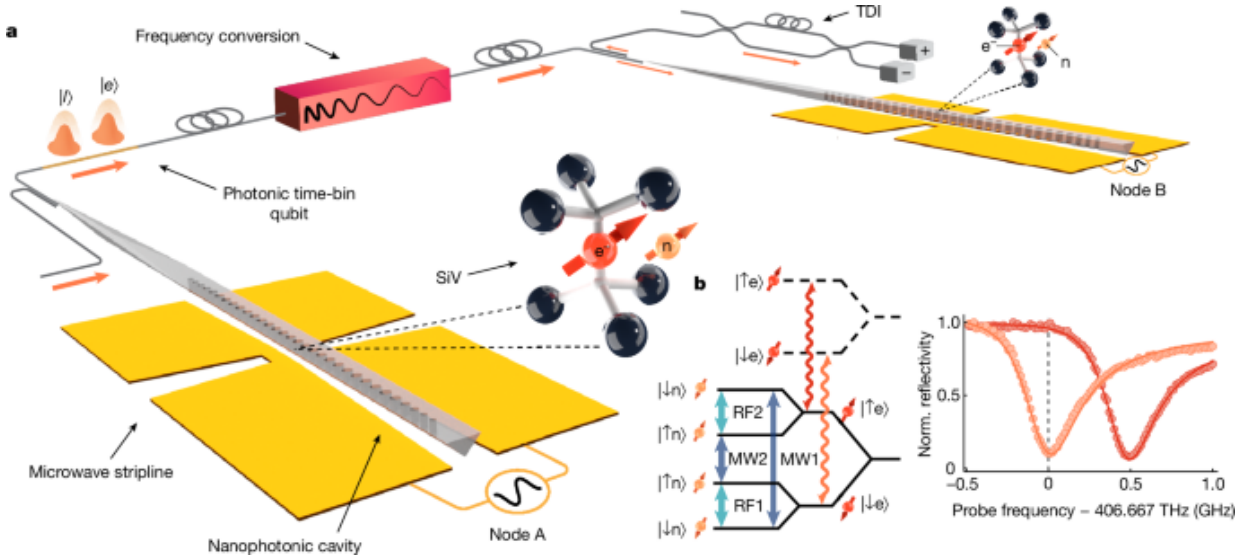

Figure 3.2: SiV Quantum Memory.

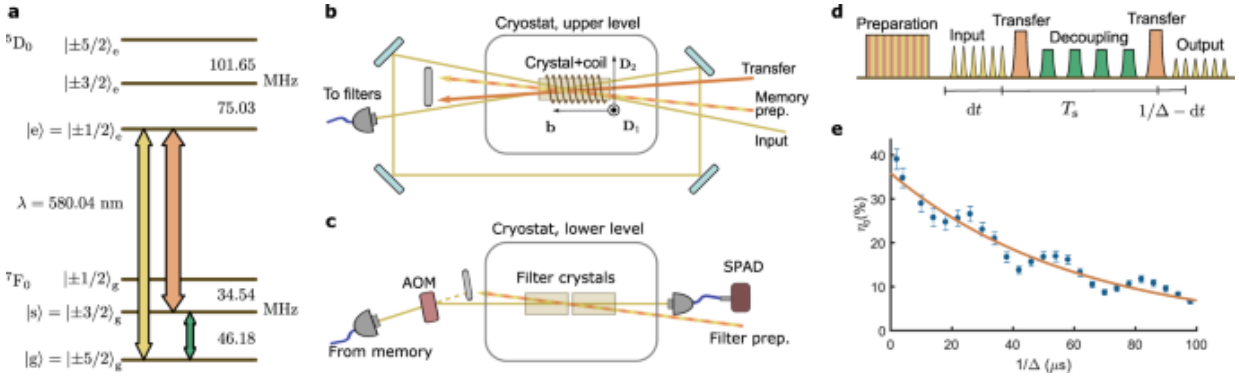

Figure 3.3: Rare-Earth Ion-Doped Crystal Quantum Memory.

While warm atoms do not have the highest efficiencies, fidelities, and storage durations, they are attractive for the scalability and relative lack of experimental complexity in a quantum network. For the remainder of the thesis, we will only consider neutral atom systems.

3.4 Quantum Memory Review: Key Findings

After parsing through several papers on quantum memories in neutral atom systems, the following key findings are a compilation of knowledge and insight for constructing quantum memories. After, we will highlight papers for their performance and discuss critical details.

- Optimal retrieval efficiency requires complete time reversal of the system dynamics (i.e. retrieval is the reverse process of storage) [38].
- Given OD, δ, and a spin wave S, one can always find a control $\Omega_c(t)$ that maps S to any desired normalized output mode $\hat{\mathcal{E}}_2(t)$ of duration T_{out} provided in the adiabatic limit [61].
- The maximum retrieval efficiency of any given stored spin-wave depends only on the optical depth, OD of the medium, which is maximized in the infinite limit of OD [61].
- An efficiency above 50 percent and fidelity above 2/3 is a necessary condition for a memory to operate within the no-cloning regime without post-selection [62].
- A 1% increase in efficiency increases entanglement distribution rate by a value beyond 10% in a repeater-based quantum network [51].
- The control laser must be stronger than the spontaneous emission rate or decoherence rate in the excited state and contain the signal field spatially [41].
- In a vapor cell, the efficiency improves as the ratio between the beam area and the cell area ($\pi w^2/L^2$) increases [**?**].
- Cell-wall anti-relaxation coating onto the inner surface of the cell may provide an effective approach to extend the memory lifetime of warm atom to the scale of milliseconds [63].

- To preserve atomic ground-state polarization, fill the vapor cell with chemically inert buffer gas or use anti-relaxation wall coatings (AWC) to prevent the depolarization from wall collisions [64].

3.4.1 Paper 1: Light Storage for One Second in Room-Temperature Alkali Vapor

The record for the longest coherent storage duration in a neutral atom system is 1 second and was realized in a room-temperature cesium vapor [37]. The experiment utilized the Zeeman coherence $\Delta m_F = 1$ associated with the spin orientation moment which is unaffected by spin-exchange collisions at low magnetic fields [37]. Spin-exchange collisions occur when two atoms come into close proximity and their spins overlap for a few picoseconds. During this time, the spins accumulate a relative phase between the singlet and triplet electronic spins. Although the total spin of the system is conserved, the system decoheres and limits the storage duration [37].

The spin-exchange immunity from the $\Delta m_F = 1$ scheme is highly sensitive to beam misalignment and stray magnetic fields. Figure 3.4 displays three configurations for transitions for the yellow signal field and the red control field. From left to right, there is the $\Delta m = 2$ Zeeman coherence, $\Delta m = 0$ hyperfine coherence, and $\Delta m = 1$ Zeeman coherence.

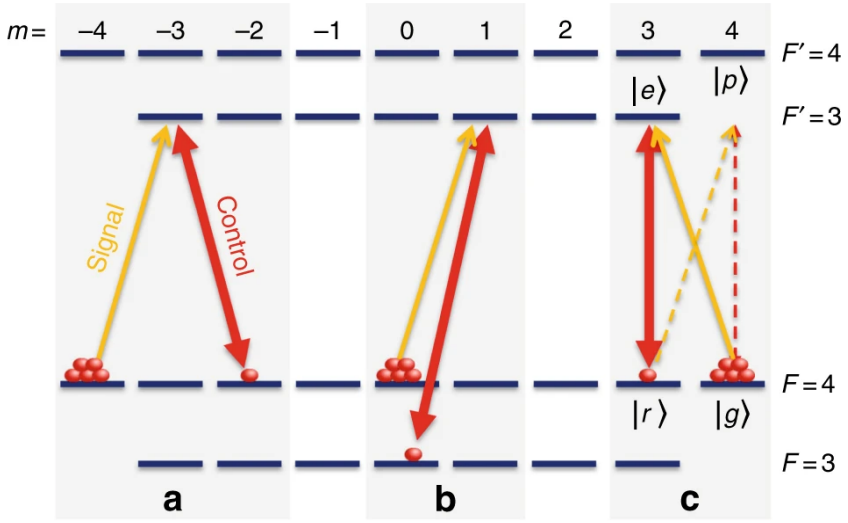

Configurations of light storage on the cesium ground-level. **a** Zeeman coherence $|\Delta m| = 2$. **b** Hyperfine coherence $|\Delta m| = 0$. **c** Zeeman coherence $|\Delta m| = 1$, associated with spin orientation, used here. The dashed arrows represent an additional weak process, discussed in the text. In ^{133}Cs, the ground and excited state hyperfine splittings are 9.19 and 1.17 GHz respectively, and the Doppler width of the optical linewidth is 370 MHz at $T = 40$ °C. Note that the signal is stored and retrieved as a linearly-polarized field, despite the fact that only one of its circular-polarization components (solid yellow line) enters the Λ-system $|g\rangle - |e\rangle - |r\rangle$, see Methods

Figure 3.4: Spin-Exchange Collision Free Transition for $\Delta m = 1$

The control field must be filtered from the signal field and the beams in a Λ memory scheme should be aligned to be practically co-propagating, which appears to be a problem in figure 3.4. Despite the fact that only one of the circular-polarization components of the signal field enters the Λ-system, the signal is fully stored and retrieved as a linearly polarized field [37]. According to Katz, under the reduced Maxwell equations, the normal modes of the susceptibility tensor comprises only components in the transverse plane. This allows the signal mode, which is fully contained in the transverse field, to be stored and retrieved as a whole. This comes at the expense of a reduced optical depth by a factor of the Clebsch-Gordan coefficient of the $|g\rangle$ to $|e\rangle$ transition.

Without optimizing the pulse shape, Katz demonstrated a modest 14% efficiency with only polarization filtering and coherent nature of the storage, but did not measure the fidelity. The experiment utilized a paraffin-coated vapor cell, magnetic field better than $|B| < 1\mu G$ measured with spin-exchange relaxation-free mechanism.

The optical pumping in this configuration adds experimental complexity. The optical

pumping polarizations are circular, but share the same axis as the linearly polarization signal and control fields. The spins orient toward the optical axis, but must be rotated to the quantization axis by a $\pi/2$ magnetic pulse orthogonal to both the quantization and optical axes.

The experiment benefited from the $\Delta = 1.17$ GHz splitting between excited state levels compared to the $\Gamma = 185$ MHz Doppler half-linewidth. The experiment can be improved by using the hyperfine ground states, even allowing for single photon storage and retrieval without losing spin-exchange immunity.

3.4.2 Paper 2: Efficient quantum memory for single-photon polarization qubits

The record for the highest coherent storage duration in a neutral atom system is 87% and was realized in a ^{87}Rb MOT [51]. The efficient single-photon quantum memory is realized with cold atoms in a dark-line MOT configuration to increase the OD to ≈ 300. The maximum storage duration was $15\mu s$ with a fidelity of 99%. Figure 3.5 displays the experimental setup.

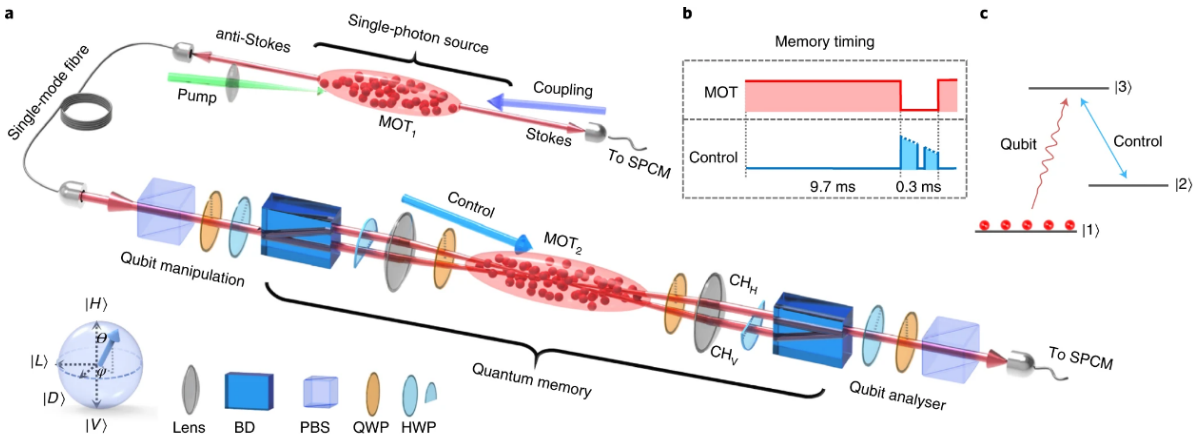

Figure 3.5: Efficient Quantum Memory in a MOT Experimental Setup

The paper addresses overcoming two challenges: suppressing noise and FWM to store single photons and producing single photons with controllable spectral-temporal states. To

address the former, the experiment set an angle of 2.2° between the control and signal fields. The angle creates an relatively large Δk, which is problematic in vapor cells due to the thermal motion.

A key insight of this experiment is their multiplexed dual-rail scheme which converts $|H\rangle$ and $|V\rangle$ to two spatial modes stored in the medium, named channels in this paper. The results for both channels are in figure 3.6.

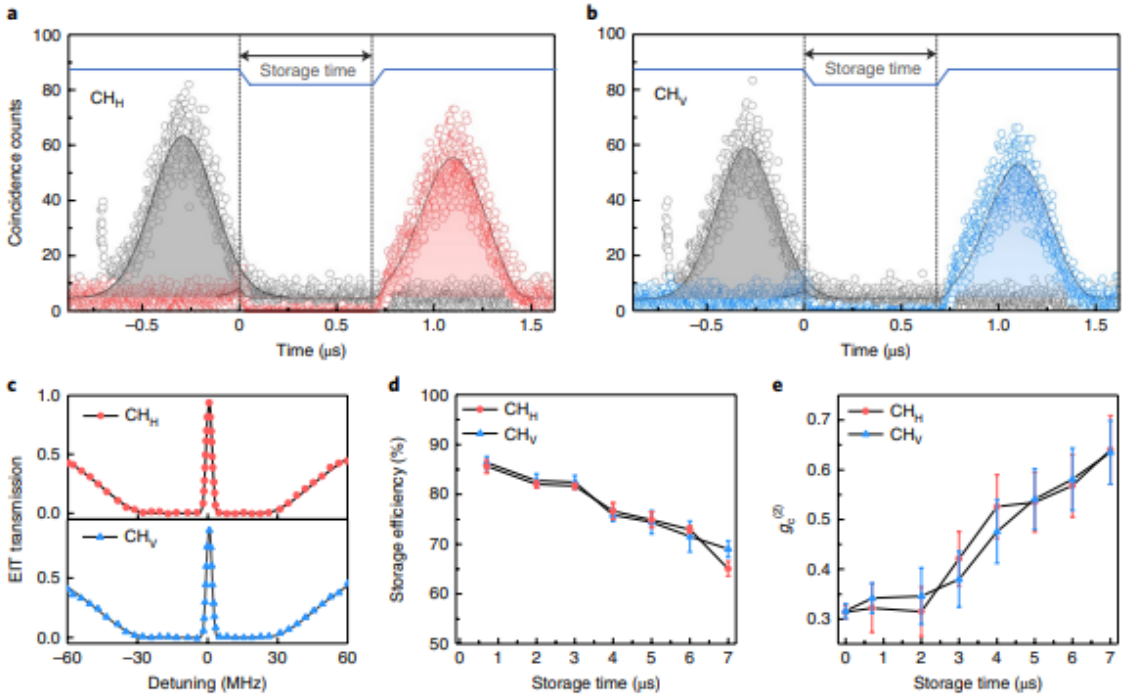

Figure 3.6: Storage Duration, EIT transmission, and Efficiency Data for the Efficient Quantum Memory

Chapter 4: Experimental Setup

4.1 Single Photon Sources

An outstanding goal of quantum memories is to store light from a different species. The goal of the experiment is to store a single photon emitted from the ion in a quantum memory for networking purposes.

4.1.1 Trapped Ion Emitted and Entangled Photon

The Quraishi group generates ion-photon entanglement by first optically pumping $^{138}Ba^{+}$ to the $5D_{3/2}$ $m_j = 3/2$ state using π-polarized 493 nm light and π-polarized and σ^{+}-polarized 650 nm light [65]. Secondly, a π-pulse of σ^{-}polarized light at 650 nm to excite the ion to the $6P_{1/2}$ state, and allowing spontaneous decay via the two dipole transition allowed paths. The emitted photon's polarization is entangled with the ion's spin: π-polarization with $m = 1/2$ and σ^{-}-polarization with $m = -1/2$. The branching ratio of the $m = -1/2$ state to $m = 1/2$ state is 2. A 0.6 NA objective positioned orthogonal to the quantization axis collects approximately 10% of the light. Due to the radiation pattern from the position of the objective, the π and σ^{-} light appear as horizontal and vertical polarizations. The entangled state is

$$\Psi = \frac{1}{\sqrt{2}}(|0H\rangle + |1V\rangle). \tag{4.1}$$

Figure 4.1 depicts the process outlined above.

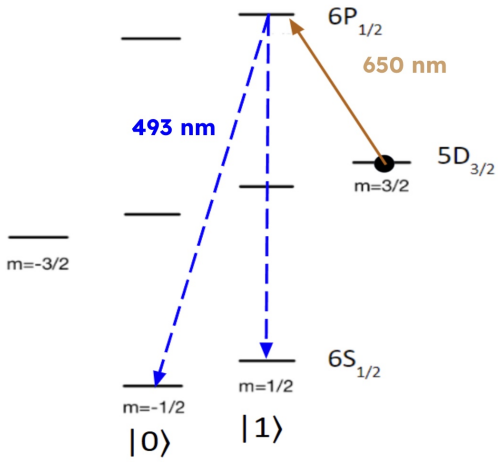

Figure 4.1: Ion-Photon Entanglement

After ion-photon entanglement is geneated, the 493 nm photon is fiberc coupled and sent to the first stage of quantum frequency conversion (QFC). A periodically poled lithium niobate waveguide (PPLN) frequency converts the 493 nm photon to 780 nm while preserving the quantum entanglement using a three-wave parametric $\chi(2)$ nonlinearity [66]. The QFC generates an output photon via optical difference frequency generation (DFG) between a pump and input photon [66]. With a tunable pump, we have the ability to tune the wavelength of the emitted photon by several hundreds of picometers. Figure 4.2 shows the experimental setup to frequency convert entangled photons to 780 nm [67].

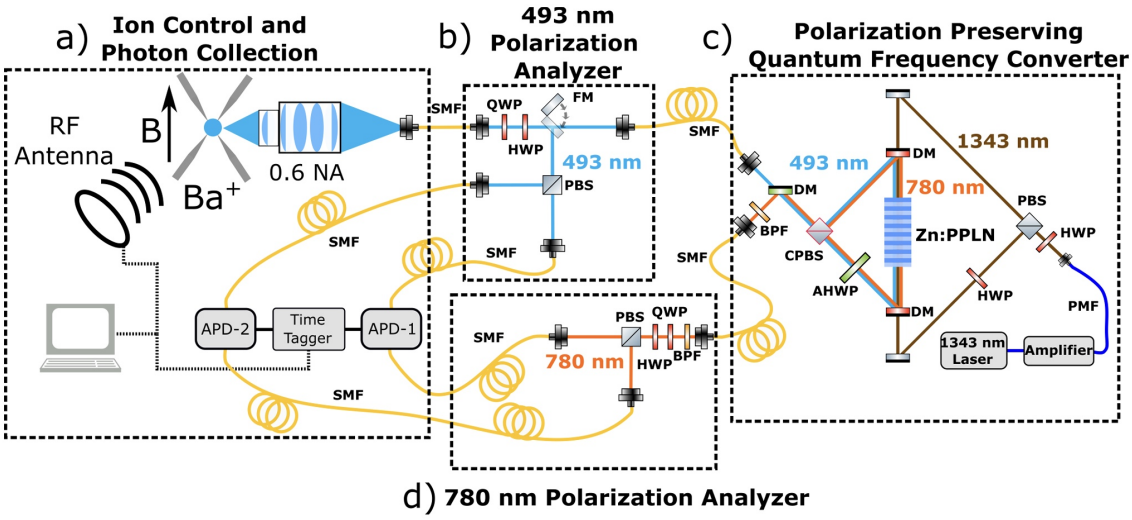

Figure 4.2: Quantum Frequency Conversion

With photons entangled with ions at 780 nm, we can interface with neutral atom systems to propel quantum networking.

4.2 Experimental Setup

Every element of the experimental setup had been carefully selected over tens of iterations and optimized to require minimal optics. The experimental setup has several advantages to include both frequency and polarization filtering, a custom vapor cell, three layers of μ-metal shielding with 1575x attenuation of magnetic fields, a multiplexed dual-rail scheme converts $|H\rangle$ and $|V\rangle$ to two spatial modes to drive one optical transition, three axes of coils in the Helmholtz configuration, heating up to 80°C, and EOMs and AOMs for amplitude and frequency modulation. The vapor cell is a scalable option for quantum memories enriched with ^{87}Rb, 10 mm length, 11 mm outer-diameter, 10 Torr Neon buffer gas, paraffin/alkene coatings, 2° wedged windows, anti-reflection (AR) coating, and a 12 mm cold finger to prevent condensing on cell windows. Figure 4.3 displays the experimental setup.

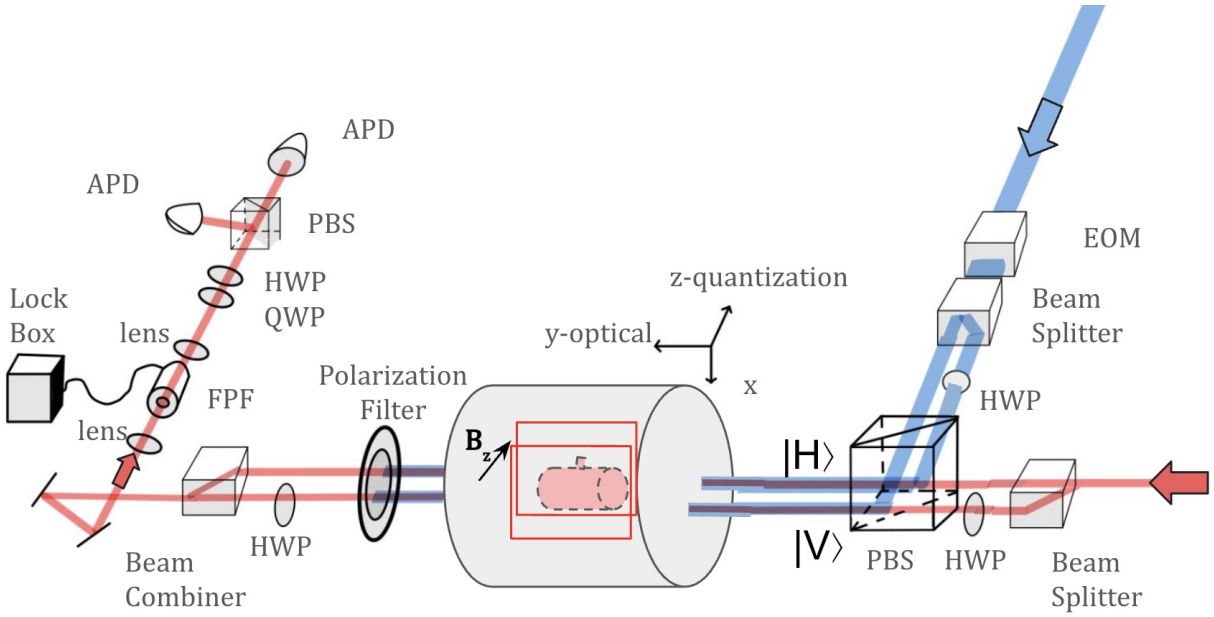

Figure 4.3: Experimental Setup

The test signal field (red) and control field (blue) are prepared prior to what is displayed in figure 4.3 in double pass configurations through free-space Isomet AOMs. The beam waist of the signal field is focused at the AOM aperture to 57 μ to decrease the rise time at the expense of AOM diffraction efficiency. The rise time is < 50 ns and 10 % is coupled into the optical fiber (80.5% fiber coupling efficiency). The control has a beam waist of 115 μm and has an 82% fiber coupling efficiency.

The control field passes through an EO-Space electrical optical phase modulator, with the capability of adding sidebands at GHz frequencies using a TTL switch. The sideband frequency is tunable, but currently operates at a single frequency during the experiment duration. Both the control and signal pass through a Thorlabs calcite prism (PN: BD27) splitting H and V polarizations into two parallel beam paths (< 30 arcseconds) separated by 2.7 mm to fit inside the vapor cell. The calcite prism is mounted on a rotation mount to optimize the rotation angle for storage. Directly after, a 5mm x 5 mm x 1 mm micro-optic half-wave plate with the fast axis 45 degrees with respect to the H-V plane rotates the polarization into the orthogonal polarization. Similarly, the control field is split with

another calcite prism, and the control's H polarization is rotated into V by another precision micro-optics waveplate. A PBS combines with control and the signal while also ensuring the polarizations are orthogonal prior to entering the quantum memory. Setting the control's polarization to be orthogonal to that of the signal, the control may co-propagate with the signal and subsequently polarization-filtered. The control and signal fields are completely overlapped in each rail, checked by inserting a removable HWP prior to the vapor cell and coupling both to the Fabry-Perot filter cavity.

There are three layers of μ metal shielding around the vapor cell, with three axis of coils. During the experiment, we plan on only applying a bias magnetic field in the Z-direction on the order of a few Gauss. There is a heater on the inside to warm the vapor cell above room temperature. At room temperature, the rubidium is condensed on the windows and cold stem. Heating creates a vapor that allows observance of the F = 1,2 absorption peaks. The maximum operating temperature is 80°C, so that the paraffin and alkene coatings do not deteriorate. After the vapor cell, a Thorlabs linear polarizer (PN: LPVIS050-MP2) with $> 10^7$ extinction ratio and 80% transmission blocks any detectable optical power by a Thorlabs photodiode power sensor (PN: S120C) with nW resolution. Following the polarizer, another precision micro-optic HWP and calcite prism mirrors preparation process and recombines the dual rails into a single beam with both polarizations. The beam passes through a Thorlabs piezo-tunable narrow bandpass Fabry-Perot filter with finesse > 300, 30 GHz FSR, 30 dB extinction, and $> 80\%$ transmission. Finally, the signal field enters the qubit analyzer, composed of a QWP, HWP, PBS, and two avalanch photodiodes (APDs) optimized for low dark count rates < 100 Hz at the expense of quantum efficiency $\approx 50\%$.

4.3 Laboratory Equipment Characterization

As an experimentalist, several technologies in my setup must be characterized prior to use. This section is dedicated to describing that characterization. Further information

on materials, checklists, and procedures can be found in the appendix.

4.3.1 Saturated Absorption Spectroscopy

To stabilize the lasers to an absolute standard, I built two Dopper-free saturated absorption spectroscopy (SAS) setups. One of the setups is shown in figure 4.4.

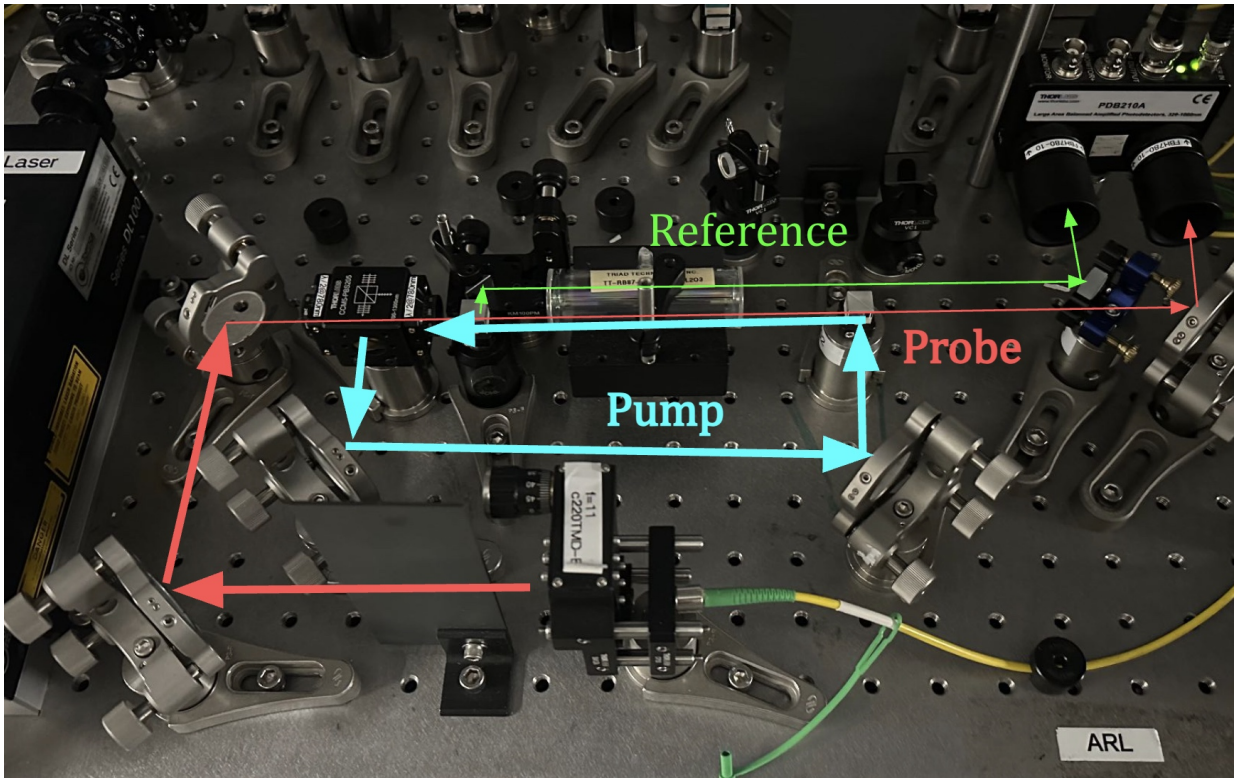

Figure 4.4: Saturated Absorption Spectroscopy Trace

Due to the physics of SAS being well known, I will not cover it in this thesis. The probe passes through an enriched ^{87}Rb vapor cell and a counter-propagating strong pump beam saturates the 0 velocity class. Parallel to the probe, a reference beam propagates through the same Rubidium cell, to obtain an absorption peak. A balanced photodetector subtracts the probe signal from the reference to create an error signal. A PID in the DLC frequency stabilizers the laser. Figure 4.5 shows a trace of the error signal for the F = 2 resonance peak.

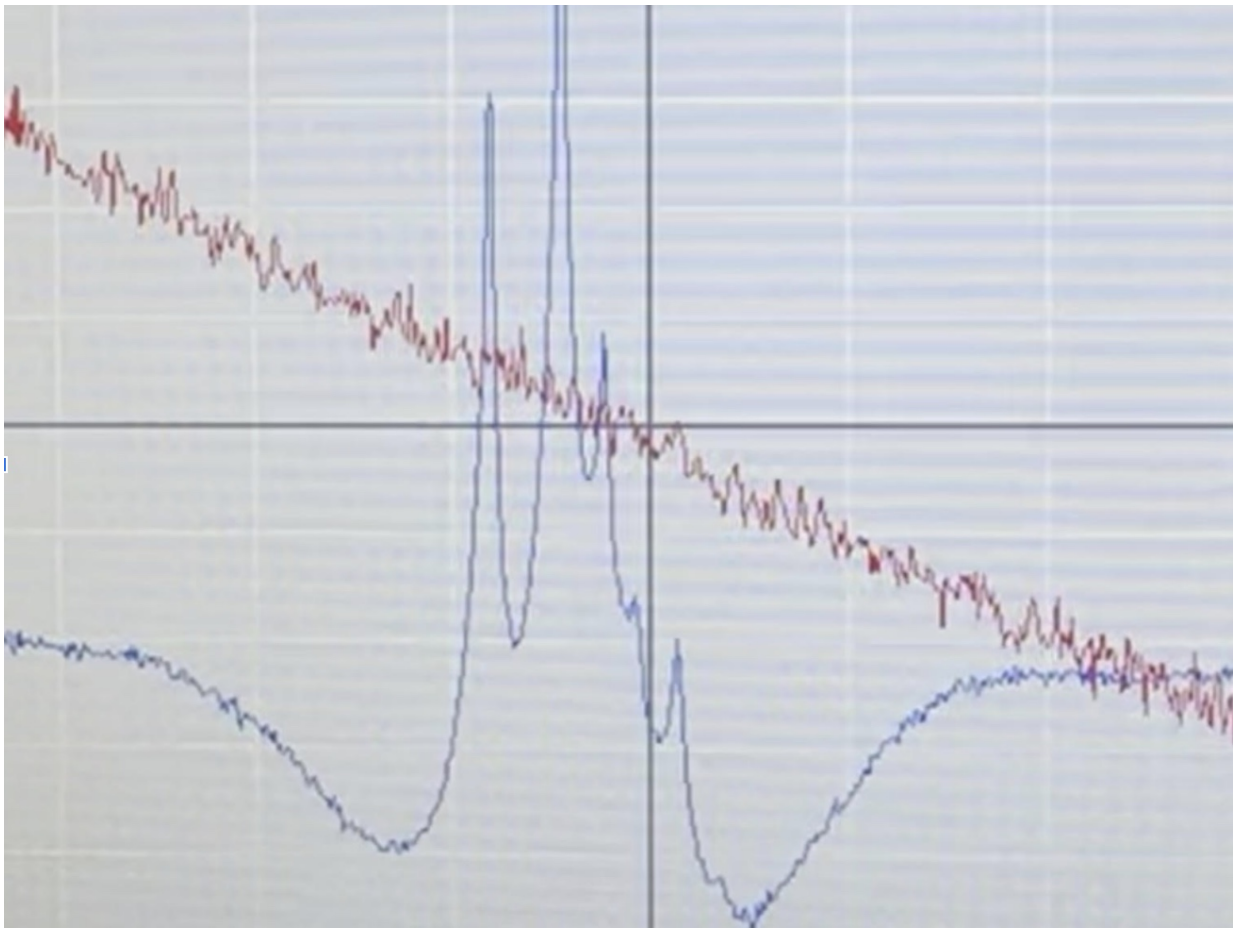

Figure 4.5: Saturated Absorption Spectroscopy Trace

4.3.2 Acousto-Optical Modulator

The acousto-optical modulator (see appendix A for more details) modulates the frequency of light and can be used to pulse shape. Using Artiq, we can control the RF frequency, RF amplitude (via attenuation), and TTL signals. In the setup, all AOMs operate at a fixed frequency throughout the duration of the experiment, but not a fixed RF amplitude. Figure 4.6 plots the attenuation in dB on the x-axis versus the optical power on the y-axis for the signal (blue) and control (red).

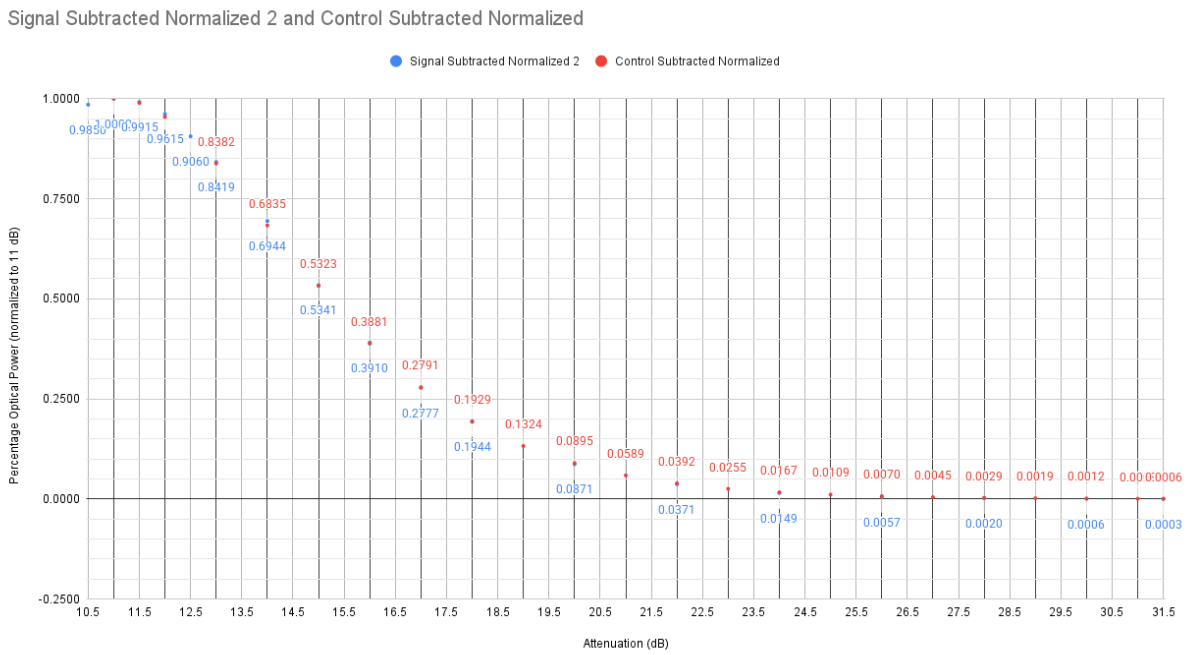

Figure 4.6: AOM Characterization

4.3.3 Electrical-Optical Modulator

The electrical-optical phase modulator (see appendix B for more details) modulates the frequency of light. While AOMs typically produce tens of MHz sidebands, EOMs can produce GHz sidebands. In the experiment, the EOM is used to create sidebands on the order of the hyperfine splitting in ^{87}Rb which is approximately 6.8 GHz. For optical pumping, the optical power ratio between the first order and carrier frequency is highly advantageous to know. Figure 4.7 plots the EOM drive power in dBm compared to the optical power ratio between the first order and carrier frequency, and compares with theory. This is measured after coupling the control beam passing through the EOM to the Fabry-Perot Filter (FPF), scanning the FPF length, and measuring the relevant amplitudes on the oscilloscope trace.

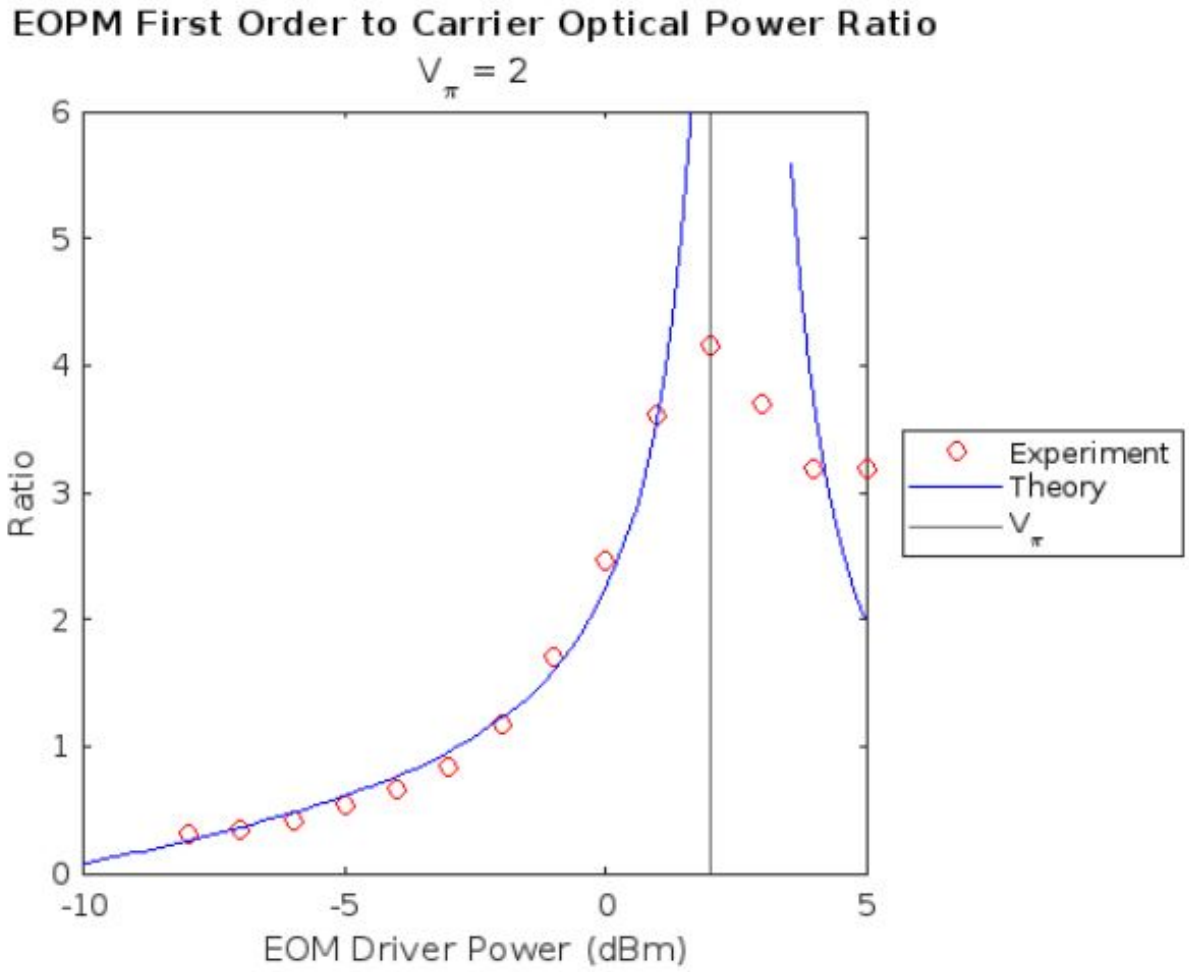

Figure 4.7: EOM Characterization

4.3.4 Magnetic Field Coils

The magnetic field coil for the optical axis was purchased as deGaussing coil with the μ-metal shielding. The magnetic field coils on the x and z axes are hand-wound around the vapor cell mount (Thorlabs PN: CBB1). Figure 4.10 are plots of the magnetic field in Gauss versus the current, in Amps, passing through the coils.

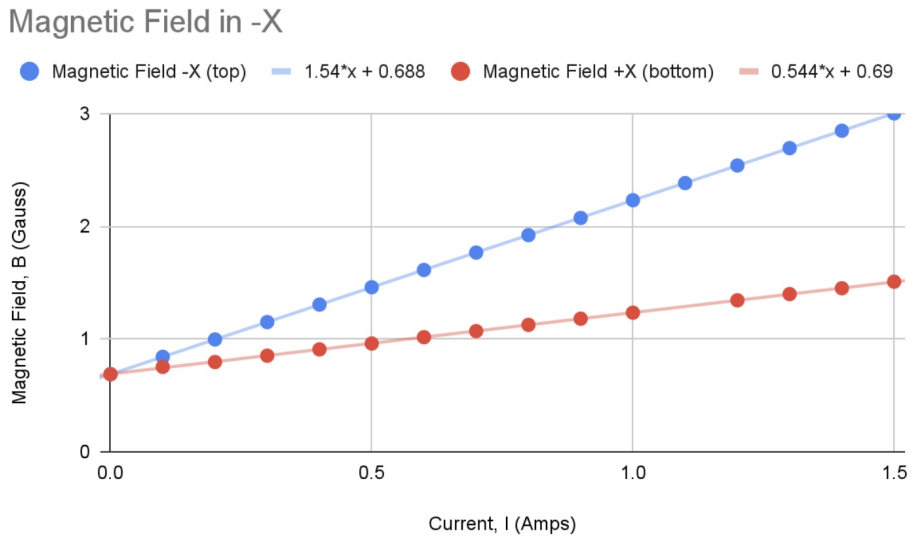

Figure 4.8: Magnetic Field in X

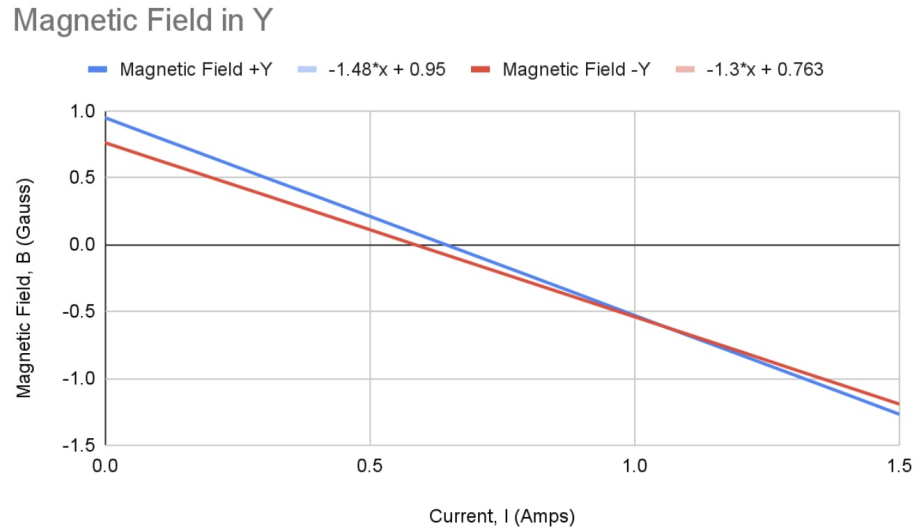

Figure 4.9: Magnetic Field in Y (optical axis)

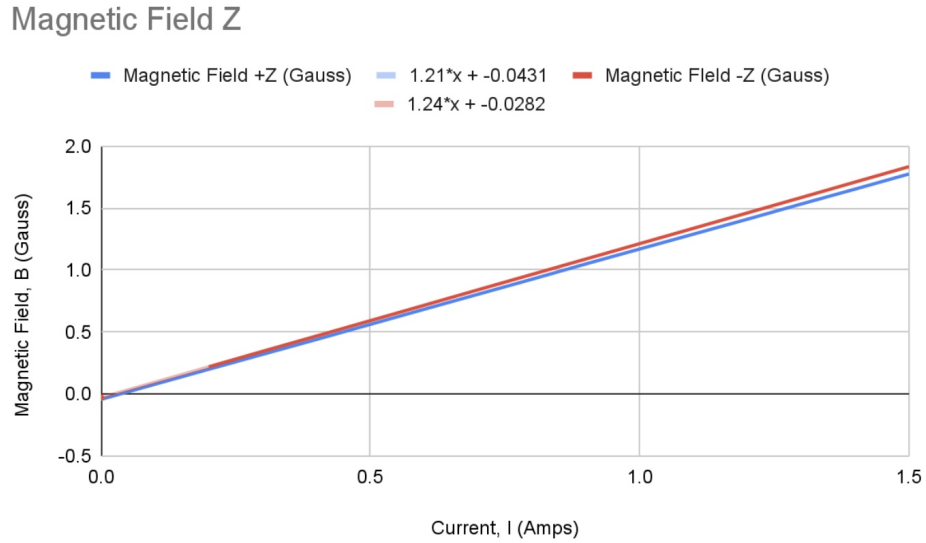

Figure 4.10: Magnetic Field in Z (quantization axis)

4.4 Transitions

4.4.1 Dipole Transitions

The quantum memory operates on the ^{87}Rb D_2 line at 780.2 nm in a warm atomic vapor. In the majority of other quantum memory schemes, the D_1 line at 795 nm for Rubidium and 852 for Cesium is used for the large excited state hyperfine splitting on the order of 1 GHz; the large splitting greatly reduces errors due to off-resonant coupling and is greater than the Doppler broadening. The D_2 line, however, is preferable to demonstrate a high efficiency quantum memory since protocols exist that use the D_2 line to generate atom-photon entanglement [68]. To enable entanglement swapping using the Hong-Ou-Mandel protocol, two indistinguishable photons that are each entangled with their respective sources must be simultaneously interfered on the same non-polarizing beam splitter. Thus, it is attractive for a quantum memory to be able to store photons at the natural frequency emitted the atom-photon entanglement scheme naturally emit photons at 780 nm.

To store the quantum state of the flying qubit in the quantum memory, the electronic state of the Rubidium atoms in the vapor cell is initialized to the $|F = 1, m_F = 0\rangle$ state. Due to Doppler broadening of the medium and the close spacing of the $D2$ lines, a certain velocity class must be selected to drive the transitions, effectively dictating the detuning from resonance.

For the given velocity class, optical pumping is used to prepare the initialized state. Driving the transitions in figure 4.11, the pump couples the $|F = 1, m_F = \pm 1\rangle$ ground state with the $|F' = 0, m_F = 0\rangle$ excited state. After being excited to the $|F' = 0, m_F = 0\rangle$ state, the electron can spontaneously decay with equal probability down to any of the $|F = 1, m_F = 0, \pm 1\rangle$ ground states. Thus for the selected velocity class, electrons starting in any of the $|F = 1, m_F = 0, \pm 1\rangle$ ground states and coupled to the $|F' = 0, m_F = 0\rangle$ state will eventually get captured in the $|F = 1, m_F = 0\rangle$ state, given a sufficient optical pumping duration.

Due to off resonant coupling, some of the electrons in the $|F = 1, m_F = 0, \pm 1\rangle$ ground states will couple with the $|F' = 1\rangle$ excited state, which is only separated by 72 MHz. Electrons that are coupled with the $|F' = 1\rangle$ excited state will spontaneously decay down to any of the $|F = 1, 2\rangle$ ground states, with decay probabilities according to the Clebsch-Gordan coefficients. The rate of the off resonant coupling is suppressed by the inverse detuning squared, hence driving the pump on resonance will limit errors due to off-resonant coupling.

If any of the electrons start or decay into the $|F = 2\rangle$ ground state, a strong repump, driven for sufficient duration, will effectively deplete the $|F = 2\rangle$ ground state population. Together with the pump, the Rubidium atoms will be prepared in the $|F = 1, m_F = 0\rangle$ state.

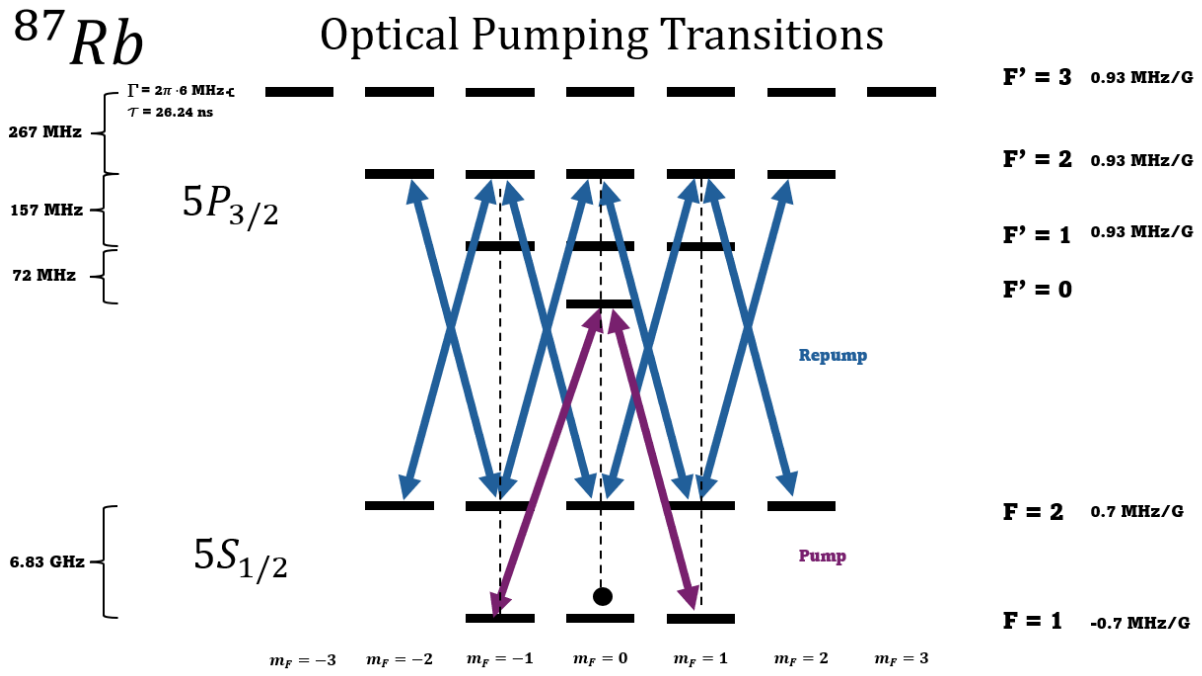

Figure 4.11: Dipole Transitions for State Preparation

It is important to note that a third transition shown as a dotted black line is weakly driven to lock the Fabry-Perot filter. Although this dipole transition removes some of the

population from the $|F = 1, m_F = 0\rangle$ state, the net effect actually helps the optical pumping process. The population in the $|F = 1, m_F = \pm 1\rangle$ states is also further reduced, and the decay from the $|F' = 2, m_F = \pm 1\rangle$ excited states to the $|F = 1\rangle$ ground state has equal probability for the $|F = 1, m_F = 0, \pm 1\rangle$ sublevels as seen in Figure 4.12. Furthermore, the decay from the $|F' = 2, m_F = 0\rangle$ is more likely to end up in the $|F = 1, m_F = 0\rangle$ than the $|F = 1, m_F = \pm 1\rangle$ states. Therefore, the addition of the third transition will not negatively impact the optical pumping process. Below in figure 4.12 are the Clebsch-Gordan coefficients for the $D2$ line.

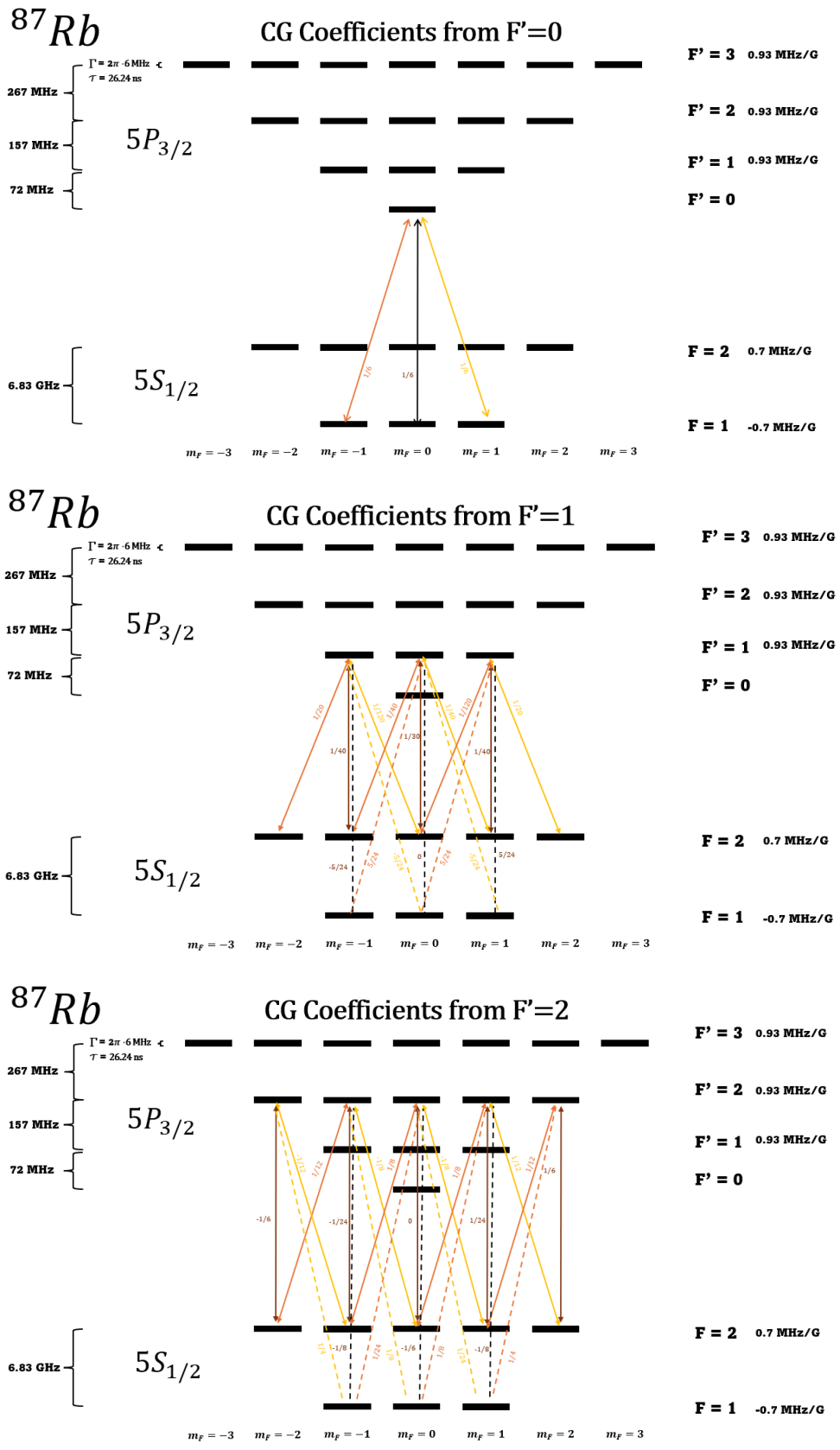

Figure 4.12: Clebsch-Gordan Coefficients for Transitions from F'= 0, 1, and 2

The selection rules of the ground and excited state hyperfine levels are exploited in the quantum memory storage scheme. In figure 4.13, the signal couples the $|F = 1, m_F = 0\rangle$ ground state with the $|F' = 2, m_F = 0\rangle$ excited state, and the control couples the $|F = 2, m_F = \pm 1\rangle$ ground states with the $|F' = 2, m_F = 0\rangle$ excited state.

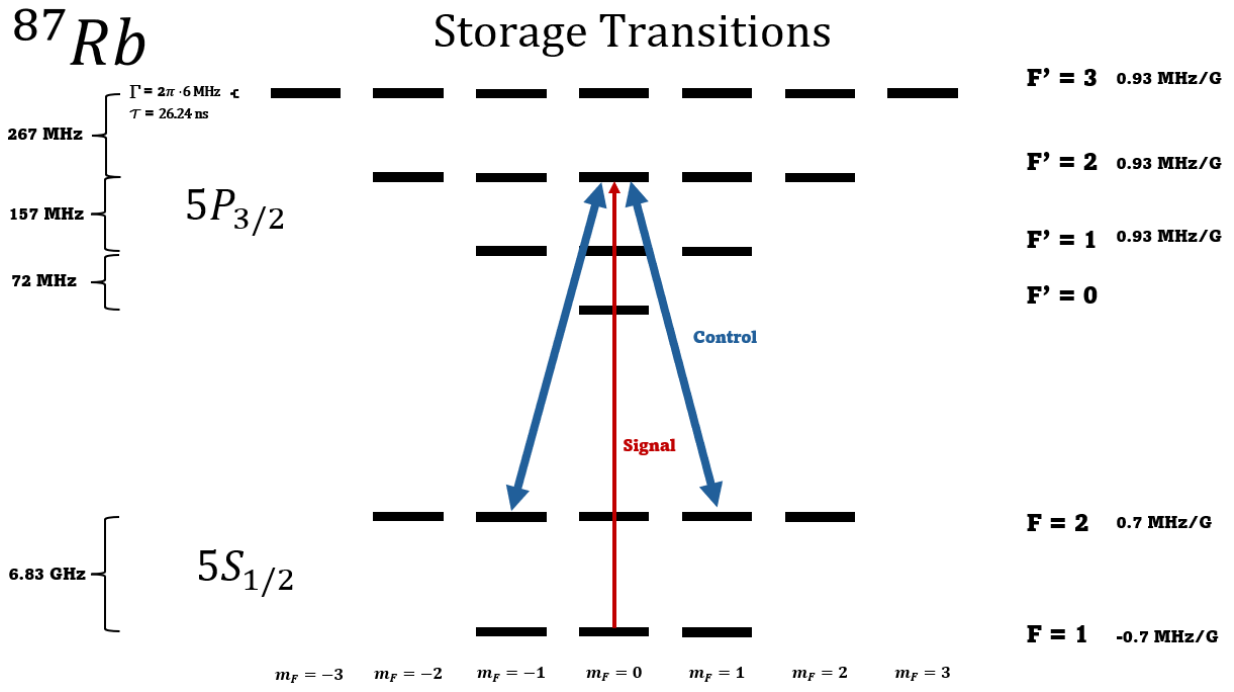

Figure 4.13: Dipole Transitions for Storage

This memory scheme has several advantages compared to previously used schemes: four-wave mixing noise and parasitic single-photon transitions are suppressed, and selections rules limit errors due to Doppler broadening. The four-wave mixing noise suppression is attributed to the 6.8 GHz splitting between the F = 1 and F = 2 ground states, which virtually prevents the control from coupling to our optically pumped $|F = 1, m_F = 0\rangle$ ground state. A parasitic single-photon transitions occurs when the signal is absorbed on a transition that requires a selection-rule forbidden mapping to the storage state $|F = 2, m_F = \pm 1\rangle$ by the control [39]. Since the control couples different m_F sublevels (i.e. $\Delta m \neq 0$), parasitic

single-photon transitions will not occur in the storage scheme, unless the signal is absorbed by 229 MHz redshifted $|F' = 0, m_F = 0\rangle$ state.

Typically for the D_2 transition, Doppler broadening with closely spaced excited state hyperfine levels significantly contributes to off resonant coupling. Due to selection-rule forbidden mappings and conservation of orbital angular momentum, the signal cannot couple the $|F = 1, m_F = 0\rangle$ with the $|F' = 1, m_F = 0\rangle$ or the $|F' = 3, m_F = 0\rangle$ states. Thus, the only off resonant coupling is with the $|F' = 0, m_F = 0\rangle$ excited state, which is approximately 229 MHz red-detuned from the transition, much better than 72 MHz. Additionally, there is an error associated with off-resonant coupling of the control with the $|F' = 3\rangle$ state which is 267 MHz blue of our control frequency.

4.4.2 Experimental Control Sequence

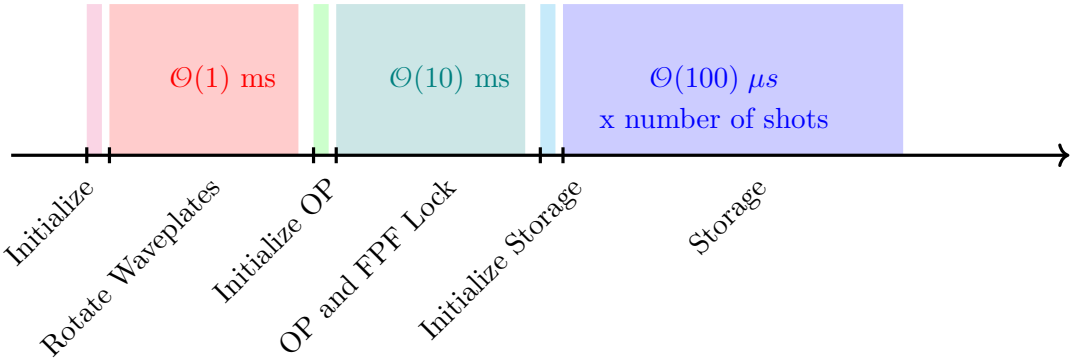

The experimental sequence consists of an optical pumping stage and a storage stage. During the optical pumping stage (OP and FPF Lock), the atomic ensemble is prepared to the $5S_{1/2}$ $|F = 1, m_F = 0\rangle$ state using the dipole transitions from Dipole Transitions and the Fabry-Perot filter (FPF) is locked. During the storage stage, the single photons are stored in the warm Rubidium vapor cell via EIT and released on-demand. To calibrate the measurement in the qubit analyzer, a quarter waveplate (QWP) and half waveplate (HWP) are scanned across parameter space (Rotate Waveplates).

The following code represents the experimental control sequence:

Algorithm 1 experiment

```
initialization()
for qwp =1: (180+5)°/5° do
    for hwp =1: (360+5)°/5° do
        opticalPumping()
        initializeStorage()
        for shot = 1:number of Shots do
            storage()
        end for
        disable control tone AOM
        rotate HWP +5°
    end for
    rotate QWP +5°
end for
```

Algorithm 2 initialization

define Delays
define Frequencies
define Attenuations
Enable Lock and Hold on Fabry-Perot Filter
Disable all tones
Home Waveplates

Algorithm 3 opticalPumping

Close Optical Shutter to protect APDs
set Frequencies for Optical Pumping
set Attenuations for Optical Pumping
enable deflecting beam to lock Fabry-Perot-Filter AOM
delay 7 ms for Optical Shutter to completely close
In Parallel
Enable Locking Fabry Perot tone AOM; Enable Optical Pumping tones AOMs/EOM
End Parallel
Disable Lock and Hold on Fabry-Perot-Filter
delay $\mathcal{O}(1)$ ms for Optical Pumping
delay $\mathcal{O}(1)$ μs to prevent underflow error (may not be necessary)
In Parallel
Disable Locking Fabry Perot tone AOM; Disable deflecting beam to lock Fabry-Perot-Filter AOM; Enable Lock and Hold on Fabry-Perot-Filter
End Parallel
delay $\mathcal{O}(1)$ μs to extend optical pumping for Optical Pumping tones only
Disable Optical Pumping tones
Open Optical Shutter to start collecting data
delay 7 ms for Optical Shutter to completely open

Algorithm 4 initializeStorage

set Frequencies for Storage
set Attenuations for Storage
enable Control tone AOM for EIT storage
delay $\mathcal{O}(1)$ μs to allow Control head start over Signal

Algorithm 5 storage

Enable Signal tone AOM/Single photon
delay $\mathcal{O}(100)$ ns for Signal pulse duration (short to resemble single photons)
In Parallel
Disable Signal tone AOM/Single photon; Disable Control tone AOM
End Parallel
delay $\mathcal{O}(100)$ us for lifetime of quantum memory
Enable Control tone AOM for EIT retrieval
delay $\mathcal{O}(10)$ μs for Signal retrieval and next Control "headstart"

Chapter 5: Summary and Outlook

5.1 Summary

Throughout the past two years in research, I have learned the state of the art of the field, designed an experiment, characterized my equipment, and built my setup. The following section will describe the steps forward and future project ideas.

5.2 Near Term Outlook

In the near term, the next logical steps involve testing the quantum memory. Currently, the ion-trap is down due to technical difficulties with the oven. In the meantime, we are collaborating with another UMD lab that can generate single photons using Rydberg states [69]. We have two fibers strung between our labs from a previous collaboration, but those will need characterized.

For the quantum memory project, I will want to use my remaining time to measure the optical pumping dephasing time, EIT Linewidth at various Δ (two-photon detunings), perform weak coherent light storage, and then single photon storage.

5.2.1 Two-Way Quantum Memory

With minimal additions, the quantum memory can be upgraded for two-way communications. We would insert a PBS between the μ-metal shielding shielding and the polarization filter, mirroring the setup on the right. To establish a second arm for the reverse control field, we would have to add a fast optical switch to direct the optical power,

or add a 50:50 BS after the EOM with two AOMs and two beam splitters on either side, depending on experimental timing requirements.

5.2.2 Pulse Control

If not being used for generating a π-pulse for atom-photon entanglement in the MOT, the electrical optical amplitude modulator (EOAM) along with Artiq's arbitary waveform generator (AWG) can be used to pulse shape the control field in the quantum memory. It is helpful to restate one of the key findings: "Given OD, δ, and a spin wave S, one can always find a control $\Omega_c(t)$ that maps S to any desired normalized output mode $\hat{\mathcal{E}}_2(t)$ of duration T_{out} provided in the adiabatic limit" [61]. While efficiency may be reduced, shaping the signal may have profound implications in entanglement swapping. For example, single photons coming from two different species may be at the same wavelength, but have significantly different pulse shapes. By dynamically reading out the collective atomic excitation or spin-wave using an EOAM to shape the control field, we may pulse shape the retrieved signal. This could significantly boost entanglement rates by making two photons indistinguishable.

5.2.3 Realizing the Quantum Memory Dipole Transitions with Ion-Photon Entanglement

Unlike the Rydberg collaboration, the photon's polarization is hyper-entangled with the frequency. To realize this memory scheme, the photon hyper-entangled with the ion in both polarization and frequency degrees of freedom must instead be hyper-entangled with spatial modes and frequency. Below is an idea of how to address the 14 MHz difference between the polarization states: Directly before storage, the magnetic field is adiabatically increased to 10 Gauss parallel to the electric field of the P-polarization, defining the quantization axis and providing a 14 MHz splitting between the $|F = 2, m_F = 1\rangle$ and

$|F = 2, m_F = -1\rangle$ ground states while leaving the magnetically insensitive $|F = 1, m_F = 0\rangle$ and $|F' = 2, m_F = 0\rangle$ states unchanged. Therefore, the two lambda systems (e.g. $|F = 1, m_F = 0\rangle$, $|F' = 2, m_F = 0\rangle$, and $|F = 2, m_F = -1\rangle$ being one lambda system) will differ by 14 MHz in the two-photon transition. This is preferable since the single photon is hyper-entangled with the ion and there exists a 14 MHz splitting in the photon's frequency degree of freedom. By choosing a 10 Gauss field, each polarization will be perfectly matched with a lambda system since the two-photon detuning is zero.

5.3 Long Term Outlook

5.3.1 Nondestructive Single Photon Measurement

To significantly increase entanglement rates, a nondestructive single photon measurement is needed. Since we cannot tell if a photon emitted by the ion has been collected by the objective, survived fiber coupling, and the QFC, we have to assume each time that we had a success for the quantum memory. If instead we had a nondestructive single photon measurement, we could tell when we have a success to significantly speed up entanglement rates.

My (open) idea for a system is as follows: using a stimulated FWM process, we input a 780 nm photon and output 795 nm photons that preserves the entanglement, but leaves the Rubidium atoms in the opposite hyperfine ground state as initialized. After the FWM process, if we measure the atoms, we can tell whether or not a photon has been converted to 795 nm for storage in a quantum memory.

5.3.2 Cavity

Depending on the initial results, we may want to add a cavity. A cavity can supress unwanted noise, including FWM, and the control field [63]. Furthermore, a cavity would allow us to suppress spontaneous emission of the anti-Stokes scattering [63].

Since the acceptance bandwidth is limited by the cavity resonance linewidth, we would want a low finesse cavity. Additionally, a ring geometry is preferable as opposed to a linear cavity so we do not produce a standing wave inside the cavity (atoms diffusing into the field nodes during the storage time would not interact at retrieval) [63].

5.3.3 MOT

Using the MOT, we could perform atom-photon entanglement, NDSPM, or a quantum memory. As a quantum memory, the MOT would have a low dephasing rate and low noise [51].

Chapter A : Acousto Optical Modulator Double Pass

Acousto-optic Modulators (AOMs) rely on the acousto-optic effect to modulate the frequency (on the order of 10s of MHz), intensity (up to on the order of 100 dB), and direction of a laser beam. A piezoelectric transducer, inside the AOM, receiving an RF signal generates a sound wave that causes a traveling strain wave in the crystal. Incident light can experience Bragg diffraction via the photo-elastic effect; a traveling refractive index grating [70]. Since the strain wave frequency is that of the RF source, Bragg diffraction changes the optical frequency by the RF frequency. As a consequence, the direction of the light beam is also shifted in the direction of the strain wave. Note that the argument above is for the positive first order diffracted beam, but the same will apply for the negative first order diffracted beam.

For constructive interference, we must have

$$n\lambda_L = \Lambda(sin\theta_i + sin\theta_d) \tag{A .1}$$

where $n \in \mathbb{Z}$, θ_i is the angle between the incident light and sound wavefronts, and θ_d is the angle between the scattered light and sound wavefronts. Since the photon's energy is much greater than that of the sound wave, the interaction is elastic and $\theta_i = \theta_d$. Thus,

$$n\lambda_L = \Lambda sin\theta_d. \tag{A .2}$$

Equation A .2 applies for the first order diffraction beam coming from the AOM. The state of the art AOMs can transmit approximately 80 percent of light with a rise time on the

order of 10s of nanoseconds.

Operating an AOM with complete experimental control requires an RF driving source, TTL, RF switch, and amplifier. We use Artiq's 4412 DDS "Urukul" as the frequency synthesizer which has sub-Hz frequency resolution, controlled phase steps, and amplitude control. Additionally, Artriq's Sinara 2118 TTL provides the TTL signal. The RF DDS and TTL are connected to the RF switch via SMA cables, and provides the experimental control to turn off and on the AOM on the order of nanoseconds. The RF switch output is connected to a Mini Circuit's ZHL-1-2W-S+ amplifier also via an SMA cable, which provides a gain of 29 dB. Finally, the amplifier is connected to the AOM via an SMA cable. The AOM frequency and intensity can be controlled on-demand via the RF frequency and amplitude, respectively.

According to equation A .2, when Λ is changed (experimentally by varying the RF frequency), the angle between the scattered light and sound wavefronts also changes. This is particularly problematic when the experiment is sensitive to the angle of light (e.g. co-propagating beams, fiber coupling). Thus, it is desirable to setup the AOM in an RF frequency-independent configuration: the double pass.

The double pass retroreflects the first order beam through the AOM for a second pass, accumulating a frequency change of twice the RF frequency. The setup for a double pass AOM is shown in figure A .1 and alignment process is described below [71]:

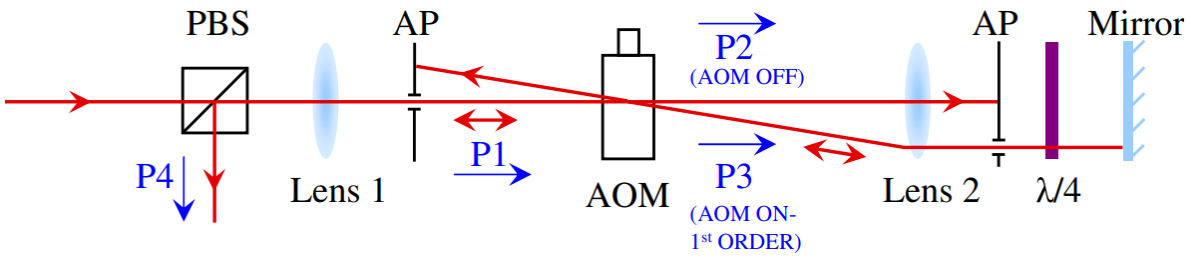

Figure A .1: AOM in Double Pass Configuration taken from D. McCarron's Guide

Quick tips:

- Placing the PBS on a tip/tilt mount may be beneficial for alignment by making sure the reflected beam's vertical and horizontal alignment downstream is also unchanging.
- It is acceptable to place lens 1 can be in a fixed mount, but helpful to place lens 2 in a z-axis translation mount.

Directions:

1. Align the beam to pass through the center of the polarizing beam splitter (PBS), ensuring the vertical and horizontal alignment downstream is unchanging. If the PBS is on a tip/tilt mount, ensure the reflected beam's vertical and horizontal alignment downstream is also unchanging.
2. Place lens 1 in front of the PBS with the curved surface facing the incoming beam, and ensure the position of the beam downstream is unchanging. This may require changing the height of the lens.
3. Measure the beam diameter using a beam profiler to match the optimal input beam waist for the AOM.
4. Place the AOM crystal (may require contacting the manufacturer) at the beam's focus and optimize the first order diffraction efficiency by tuning the five-axis stage.
5. Turn off the RF signal from the AOM and insert lens 2 in a translation mount (in the axial direction) at the lens' focal length from the AOM crystal. Confirm that lens 2 does not shift the beam downstream.
6. Insert a quarter waveplate (QWP) and mirror after the lens, allowing space for an aperture. The beam should pass through the center of the QWP and and reflect off the center of the mirror.

7. Place an aperture after the first lens to only pass through the incident beam to the AOM.

8. Retroreflect the zeroth order beam through the AOM (the aperture can be used as a guide).

9. Rotate the QWP to allow maximum reflection (measuring the power in the P4 direction in figure A .1)

10. Turn on the AOM and adjust the QWP so that the first (or negative first) order diffracted beam is centered.

11. Place an aperture between lens 2 and the QWP to block all other beams besides the desired beam.

12. Optimize the power P4 by fine tuning the mirror, translating lens 2, and rotating the QWP.

Chapter B: Electrical Optical Modulators

An electrical optical modulator (EOM) is a device typically made of lithium niobate crystal that changes the birefringence due to an electrical signal (typically RF). There are two main types of EOMs: electrical optical amplitude modulators (EOAMs) and electrical optical phase modulators (EOPMs). EOAMs act as a actuated PBS and waveplate combination and provide amplitude modulation. EOPMs modulate the phase of the light passing through the medium. Both EOAMs and EOPMs are typically polarization dependent devices.

An EOAM is characterized by the voltage V_π that causes a phase shift of π.

The transmission is related by

$$T = sin^2(\frac{\pi}{2}\frac{V}{V_\pi}). \tag{B.1}$$

Chapter C: Fabry Perot Filter

C.0.1 Fabry-Perot Filter

The section below is compiled from Thorlab's manual for the Fabry-Perot Filter. The Fabry-Perot Filter (FPF) is a cavity that can act as a filter for unwanted frequencies; once calibrated, the transmission is above 80 percent with a minimum of 30 dB suppression. The FPF is composed of a highly reflective planar and highly reflective spherical concave mirror. By adjusting the mirror separation using a piezoelectric transducer, the frequency of the cavity mode can be tuned as seen in figure C.1.

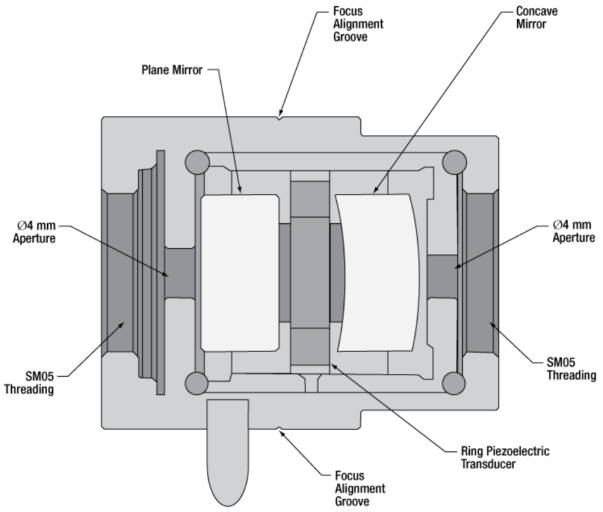

Figure C.1: Thorlabs Fabry-Perot Filter Diagram

The FPF used in the Quantum Memory experiment has a linewidth smaller than 100 MHz and a Free Spectral Range (FSR) of 30 GHz. The FSR is defined as the frequency

difference between modes given by equation C.1:

$$FSR = \frac{c}{2d} \tag{C.1}$$

where c is the speed of light and d is the cavity length. The plano-concave cavity supports a fundamental mode whose waist is on the flat mirror with a Gaussian intensity given by equation C.2:

$$I(r) = exp(-2(\frac{r}{\omega_{cav}})^2) \tag{C.2}$$

where ω_{cav} being determined by the cavity length, d, and the radius of curvature of the curved mirror, R, given by equation C.3:

$$\omega_{cav} = \sqrt{\frac{\lambda}{\pi}\sqrt{d(R-d)}}. \tag{C.3}$$

With $R = 250\ mm$, $d = 5\ mm$, and for 780 nm light, the cavity waist is approximately 93 μm. To optimize the performance of the cavity, the incident light must be near-perfectly mode matched to the cavity. To realize this, the incident light should be focused on the FPF with the spot size corresponding to the cavity waist. Experimentally, this is accomplished using a lens with focal length, f, calculated using equation C.4:

$$f = \frac{\pi\omega_0\omega_{cav}}{\lambda}. \tag{C.4}$$

The FPF should be placed exactly at the focal point, which can be accomplished by centering the lens in a translation mount of the correct height, and ensuring the beam location downstream remains unchanged. Once the correct spot size is realized, the relative orientation of the cavity with respect to the incident beam must be set. With four DOF to the orientation (e.g. horizontal and vertical location, tip and tilt), there must be at least two tip and tilt mounts to near-perfectly mode match. The alignment is performed by rotating one of the vertical knobs slightly and sweeping the other vertical knob for optimal

results, followed by the same process for the horizontal. Several iterations of this process will adequately suppress the higher order modes so that the end result looks like figure C.2:

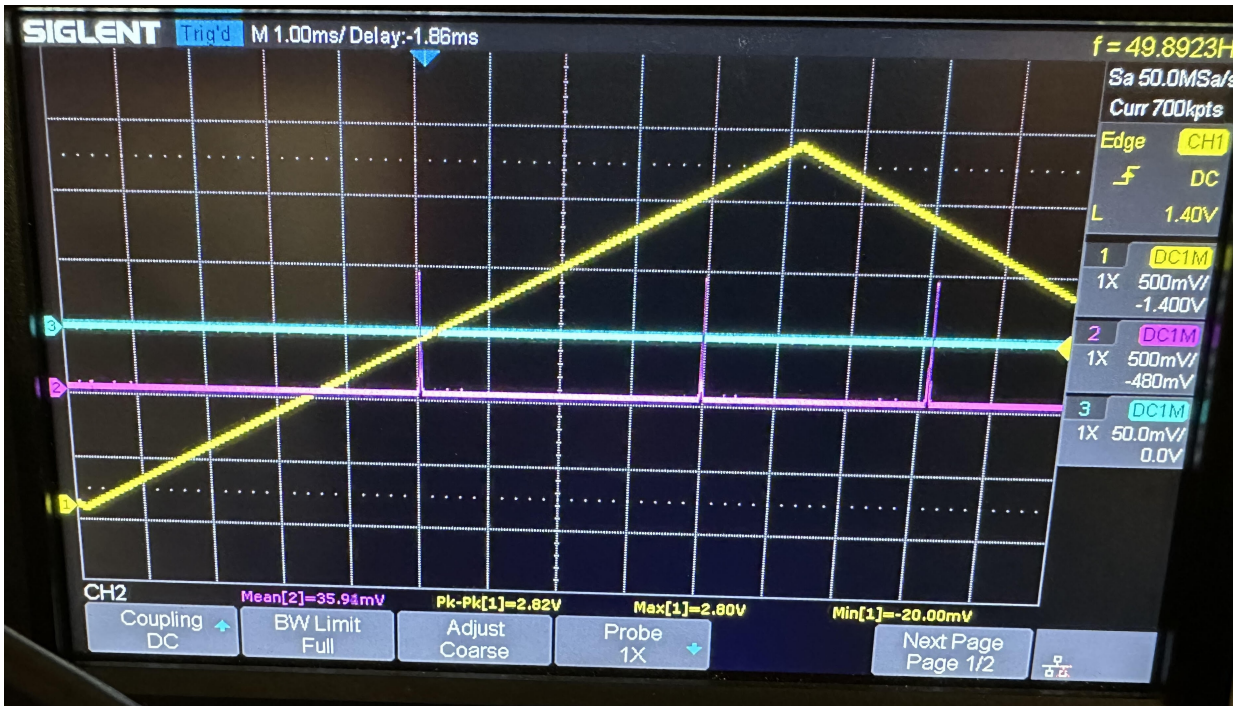

Figure C.2: Optimal FPF Coupling

This alignment process is essentially the same as fiber coupling and should conclude when the higher order modes are adequately suppressed.

Closed Feedback Loop Stabilization

A closed feedback loop is required to stabilize the FPF. Newport Photonic's LB1005 High-Speed Servo Controller contains all the required components for feedback control in one device. The LB1005 generates an error signal from the photodiode and filters this signal to provide an output voltage for the transducer input. Since the transducer used in the experiment can only take input voltages between 0 and 10 V, the output voltage limit setting is set accordingly. It is important to note that the LB1005 does not mix the signal; a Side-of-Fringe locking technique must be used instead of a Top-of-Fringe lock (e.g. Pound-Drever-Hall technique).

To lock the LB1005, the following procedure is used (which is adapted from the manual):

1. Set the Output Voltage Limit setting using the **Output Voltage Limit trimpots** located on the rear panel.

   (a) To set the positive (negative) limit, turn the **Sweep Center (Output Offset)** knob fully clockwise (counter-clockwise). The **Output** signal is now at the positive (negative) voltage limit.

   (b) Monitoring the Output voltage on an oscilloscope or voltmeter, turn the $+(-)$ trimpot on the rear panel until the desired positive (negative) output limit voltage is reached. Clockwise adjustment of the trimpots results in a more positive voltage.

2. Reset the integrator by toggling the Acquire switch to the **Lock Off** position

3. Find the locking point by sweeping over the resonance. This can be realized by connecting a 1 kHz triangle wave signal generator to the **Sweep In** input, turning the **Sweep Span** knob to allow a wide span, and centering the resonance on the center of the oscilloscope trace using the **Center (Output Offset)** knob. Monitor the **Output** voltage and find the resonance closest to the center of the output voltage limits using the **Center (Output Offset)** knob.

4. Use the **Input Offset** knob to allow the Lorentzian peak to cross the zero-point for the error signal on the oscilloscope.

5. Acquire the lock by toggling the **Acquire lock** switch to LFGL, adjusting the **Gain** while centering the resonance on the trace. Note a gain of 1.9 V was used in the locking procedure. If the LED is not green, then the **Output** voltage may be too close to the output voltage limits or the absolute value of the error signal is too high. For the former, turn the **Center (Output Offset)** knob to find the resonance closest

to the center of the output voltage limits. For the latter, adjust the **Center (Output Offset)**, **Gain**, and **Input Offset** knobs until the amplitude is decreased.

6. Slowly reduce the sweep by turning the **Sweep Span** knob to counter-clockwise while using the **Center (Output Offset)** knob to center the resonance on the trace until the lock point takes up the whole oscilloscope screen.

7. Use the **Center (Output offset)** knob to find where the error signal crosses the zero-point on the oscilloscope trace. Note that the **Center (Output offset)** knob may need to be adjusted so that the error signal is for the correct locking point as in figure **??**. The error signal should produce a "restoring force" for the transducer.

8. Toggle the Acquire switch to the **Lock On** position and tune the **Gain** until there is a resonance. Now back off the **Gain** slightly.

9. Tune the **P-I Corner** frequency to optimize the lock

During the experiment, there is a locking sequence which locks the FPF prior to several iterations of the full experiment. The LB1005 using a TTL signal to "hold" the current value. When the TTL signal is "high," the error signal input is temporarily disabled.

Chapter C: Laser Frequency Stabilization

C.1 Locking a Toptica System

C.1.1 Lock License

The simplest (and worse) is purchasing a lock license and using a saturated absorption spectroscopy setup (SAS). The lock license enables either a side of fringe lock or a top of fringe lock using the PIDs installed in the DLC (despite PIDs being already installed, Toptica prevents their use without the lock license). The top of fringe lock uses a modulation frequency anywhere from 100s of Hz to 100s of kHz (not as good as PDH). The lock can be achieved by inputting a photodetector signal into the fine (better than fast) input channel on the DLC. Hitting the scan option (left side, second to top button), the DLC automatically scans the laser frequency. With the lock license, the DLC finds lock points which can be selected and locked to via the lock button on the left. Additionally, the PID settings can be controlled in the parameters settings.

C.1.2 Pound-Drever-Hall (PDH) Lock

A better lock uses the PDH module to create an error signal for a Top of Fringe lock. The PDH module can provide a 5 MHz or 250 MHz modulation frequency for the error signal. Either an external PID or the lock license enabled PIDs can be used to lock the laser frequency using the parameter settings.

C.1.3 PDH and FALC

The PDH and FALC can be used together to create the best lock. The FALC contains all the necessary PIDs (better than the PIDs installed in the DLC which require the lock license to unlock) to lock the laser frequency. The SAS output goes into the PDH which creates an error signal using modulation that goes into the FALC. The FALC PIDs then can be used to lock the laser frequency. The lock license is not required, but helps facilitate the process.

C.1.4 PID Locking Settings to the Wavemeter

The regulation signal is a proportional, integral, and derivative device that can be optimized for frequency locking. The form of the PID regulation is

$$Output(t) = S * [P * error + I' * \int error * dt + D' * \frac{derror}{dt}] \tag{C.1}$$

where $S0$ is the sensitivity, P is the proportionality parameter, $I' = \frac{I}{t_a}$is the integral parameter where t_a is the time constant parameter, and $D' = \frac{D}{t_a}$is the derivative parameter.

Note the proportional value to the error signal will either increase or decrease the actual signal to the set signal. The derivative value will decrease the rate of how fast the actual signal approaches the set signal, which is necessary to avoid overshooting. The integral value helps avoid oscillations caused by the proportional and derivative values, analogous to a damping term in an oscillator.

The optimal P, I, D, and t_a parameter values can be found with the procedure below:

1. Open PIDSim2.

2. Set measurement count to a value between 100 and 10,000 (higher values correspond to longer simulations).

3. Click the arrows at the top right of General, Laser, and Regulation to expand all tunable parameters.

4. Click the Synchronize button at the bottom of Regulation to synchronize the wavemeter with the simulation. Allow the wavemeter to be linked with the simulation (not the other way around).

5. Change the Port value to the port of interest for locking the corresponding frequency.

6. Click the red button to the right of Time/Measurement to load real time data of the measurement cycle time.

7. Set the response count (number of cycles until the response wavelength of a regulation action is known) to 2 (typical value according to Wavelength Meter Angstrom WS Ultimate 2 user manual section 3.6.1.3).

8. Set the VOut maximum to a conservative value within the extrema of the (bnc) input voltages on the laser controller that are connected to the wave meter.

9. Set VOut resolution to 0.3 mW.

10. It is unnecessary to synchronize f and r.

11. Click the red circle next to 1/Amplification to get a live reading of the laser's wavelength.

12. A nonzero perturbation can be included to simulate external perturbations (in pm); similarly, noise and sudden hops can also be simulated.

13. Click Auto TPID to generate an ansatz for the PID settings. Note that the sensitivity may need to be changed and the Auto TPID may need to be recalculated until the simulation shows a good lock.

Chapter C: Quantum Memory Start-up Checklist

1. AOM amplifiers (above setup) - on
2. EOM amplifiers (near EOM driver) - on
3. EOM Driver (across from AOM amplifiers) - on
4. RF Switches (Artiq: Set internal RF switches) - on
5. TTLs (Artiq: Quantum Memory AOM Align) - on
6. Laser in use sign - on
7. Both 780 Lasers - on
8. Wavemeter - on
9. Heat (cart) - on
10. Degauss - reference manual
11. Magnetic field (above setup) - on
12. Oscilloscopes (next to setup) - on
13. Photodiodes (setup) - on
14. FPF locking electronics - on
15. Lock Lasers - achieve lock

Bibliography

[1] Jameson O'Reilly, George Toh, Isabella Goetting, Sagnik Saha, Mikhail Shalaev, Allison L. Carter, Andrew Risinger, Ashish Kalakuntla, Tingguang Li, Ashrit Verma, and Christopher Monroe. Fast photon-mediated entanglement of continuously cooled trapped ions for quantum networking. *Phys. Rev. Lett.*, 133:090802, Aug 2024.

[2] Xiu-Ying Chang, Pan-Yu Hou, Wen-Gang Zhang, Xiang-Qian Meng, Ye-Fei Yu, Ya-Nan Lu, Yan-Qing Liu, Bin-Xiang Qi, Dong-Ling Deng, and Lu-Ming Duan. Hybrid entanglement and bit-flip error correction in a scalable quantum network node. *Nature Physics*, April 2025.

[3] Klemens Hammerer, Anders S. Sørensen, and Eugene S. Polzik. Quantum interface between light and atomic ensembles. *Rev. Mod. Phys.*, 82:1041–1093, Apr 2010.

[4] H J Kimble. The quantum internet. *Nature*, 453(7198):1023–1030, June 2008.

[5] A R McMillan, L Labonté, A S Clark, B Bell, O Alibart, A Martin, W J Wadsworth, S Tanzilli, and J G Rarity. Two-photon interference between disparate sources for quantum networking. *Sci. Rep.*, 3(1):2032, 2013.

[6] Aishwarya Kumar, Aziza Suleymanzade, Mark Stone, Lavanya Taneja, Alexander Anferov, David I Schuster, and Jonathan Simon. Quantum-enabled millimetre wave to optical transduction using neutral atoms. *Nature*, 615(7953):614–619, March 2023.

[7] John Hannegan, James D. Siverns, Jake Cassell, and Qudsia Quraishi. Improving entanglement generation rates in trapped-ion quantum networks using nondestructive photon measurement and storage. *Phys. Rev. A*, 103:052433, May 2021.

[8] John Hannegan, James D. Siverns, and Qudsia Quraishi. Entanglement between a trapped-ion qubit and a 780-nm photon via quantum frequency conversion. *Phys. Rev. A*, 106:042441, Oct 2022.

[9] J. D. Siverns, J. Hannegan, and Q. Quraishi. Demonstration of slow light in rubidium vapor using single photons from a trapped ion. *Science Advances*, 5(10):eaav4651, 2019.

[10] Kathryn Ann Moler, Gretchen K. Campbell, Jamil Abo-Shaeer, Fred Chong, James S. Clarke, Deborah Ann Frincke, Gilbert V. Herrera, Nadya Mason, William D. Oliver, John Preskill, Mark B. Ritter, Robert J. Schoelkopf, Krysta M. Svore, Jinliu Wang, and Jun Ye. Quantum networking: Findings and recommendations for growing american leadership, 2024.

[11] Andrew M Childs and Wim van Dam. Quantum algorithms for algebraic problems. December 2008.

[12] Mar 2025.

[13] Michael A. Nielsen and Isaac L. Chuang. *Quantum Computation and Quantum Information: 10th Anniversary Edition*. Cambridge University Press, 2010.

[14] Dan C Marinescu. *Classical and Quantum Information*. Academic Press, San Diego, CA, February 2011.

[15] J. S. Bell. On the einstein podolsky rosen paradox. *Physics Physique Fizika*, 1:195–200, Nov 1964.

[16] Davide Castelvecchi. IBM releases first-ever 1,000-qubit quantum chip. *Nature*, 624(7991):238, December 2023.

[17] Daniel Gottesman. Stabilizer codes and quantum error correction. May 1997.

[18] Noah Berthusen, Dhruv Devulapalli, Eddie Schoute, Andrew M. Childs, Michael J. Gullans, Alexey V. Gorshkov, and Daniel Gottesman. Toward a 2d local implementation of quantum low-density parity-check codes. *PRX Quantum*, 6:010306, Jan 2025.

[19] Nicolas Sangouard, Christoph Simon, Hugues de Riedmatten, and Nicolas Gisin. Quantum repeaters based on atomic ensembles and linear optics. *Rev. Mod. Phys.*, 83:33–80, Mar 2011.

[20] Xueshi Guo, Casper R Breum, Johannes Borregaard, Shuro Izumi, Mikkel V Larsen, Tobias Gehring, Matthias Christandl, Jonas S Neergaard-Nielsen, and Ulrik L Andersen. Distributed quantum sensing in a continuous-variable entangled network. *Nature Physics*, 16(3):281–284, March 2020.

[21] Lixia Ma, Xing Lei, Jieli Yan, Ruiyang Li, Ting Chai, Zhihui Yan, Xiaojun Jia, Changde Xie, and Kunchi Peng. High-performance cavity-enhanced quantum memory with warm atomic cell. *Nat. Commun.*, 13(1):2368, May 2022.

[22] J. Hannegan, U. Saha, J. D. Siverns, J. Cassell, E. Waks, and Q. Quraishi. C-band single photons from a trapped ion via two-stage frequency conversion. *Applied Physics Letters*, 119(8):084001, 08 2021.

[23] L-M Duan, M D Lukin, J I Cirac, and P Zoller. Long-distance quantum communication with atomic ensembles and linear optics. *Nature*, 414(6862):413–418, November 2001.

[24] H.-J. Briegel, W. Dür, J. I. Cirac, and P. Zoller. Quantum repeaters: The role of imperfect local operations in quantum communication. *Phys. Rev. Lett.*, 81:5932–5935, Dec 1998.

[25] A Paetznick, M P da Silva, C Ryan-Anderson, J M Bello-Rivas, J P Campora, III, A Chernoguzov, J M Dreiling, C Foltz, F Frachon, J P Gaebler, T M Gatterman, L Grans-Samuelsson, D Gresh, D Hayes, N Hewitt, C Holliman, C V Horst, J Johansen, D Lucchetti, Y Matsuoka, M Mills, S A Moses, B Neyenhuis, A Paz, J Pino, P Siegfried, A Sundaram, D Tom, S J Wernli, M Zanner, R P Stutz, and K M Svore. Demonstration of logical qubits and repeated error correction with better-than-physical error rates. April 2024.

[26] Pengfei Wang, Chun-Yang Luan, Mu Qiao, Mark Um, Junhua Zhang, Ye Wang, Xiao Yuan, Mile Gu, Jingning Zhang, and Kihwan Kim. Single ion qubit with estimated coherence time exceeding one hour. *Nature Communications*, 12(1):233, January 2021.

[27] C M Löschnauer, J Mosca Toba, A C Hughes, S A King, M A Weber, R Srinivas, R Matt, R Nourshargh, D T C Allcock, C J Ballance, C Matthiesen, M Malinowski, and T P Harty. Scalable, high-fidelity all-electronic control of trapped-ion qubits. July 2024.

[28] K Wright, K M Beck, S Debnath, J M Amini, Y Nam, N Grzesiak, J-S Chen, N C Pisenti, M Chmielewski, C Collins, K M Hudek, J Mizrahi, J D Wong-Campos, S Allen, J Apisdorf, P Solomon, M Williams, A M Ducore, A Blinov, S M Kreikemeier, V Chaplin, M Keesan, C Monroe, and J Kim. Benchmarking an 11-qubit quantum computer. *Nature Communications*, 10(1):5464, November 2019.

[29] C. Monroe and J. Kim. Scaling the ion trap quantum processor. *Science*, 339(6124):1164–1169, 2013.

[30] Sepehr Ebadi, Tout T Wang, Harry Levine, Alexander Keesling, Giulia Semeghini, Ahmed Omran, Dolev Bluvstein, Rhine Samajdar, Hannes Pichler, Wen Wei Ho, Soonwon Choi, Subir Sachdev, Markus Greiner, Vladan Vuletić, and Mikhail D Lukin. Quantum phases of matter on a 256-atom programmable quantum simulator. *Nature*, 595(7866):227–232, July 2021.

[31] Simon J Evered, Dolev Bluvstein, Marcin Kalinowski, Sepehr Ebadi, Tom Manovitz, Hengyun Zhou, Sophie H Li, Alexandra A Geim, Tout T Wang, Nishad Maskara, Harry Levine, Giulia Semeghini, Markus Greiner, Vladan Vuletić, and Mikhail D Lukin. High-fidelity parallel entangling gates on a neutral-atom quantum computer. *Nature*, 622(7982):268–272, October 2023.

[32] Pascal Scholl, Michael Schuler, Hannah J Williams, Alexander A Eberharter, Daniel Barredo, Kai-Niklas Schymik, Vincent Lienhard, Louis-Paul Henry, Thomas C Lang, Thierry Lahaye, Andreas M Läuchli, and Antoine Browaeys. Quantum simulation of 2D antiferromagnets with hundreds of rydberg atoms. *Nature*, 595(7866):233–238, July 2021.

[33] Dolev Bluvstein, Harry Levine, Giulia Semeghini, Tout T Wang, Sepehr Ebadi, Marcin Kalinowski, Alexander Keesling, Nishad Maskara, Hannes Pichler, Markus Greiner, Vladan Vuletić, and Mikhail D Lukin. A quantum processor based on coherent transport of entangled atom arrays. *Nature*, 604(7906):451–456, April 2022.

[34] Richard Bing-Shiun Tsai, Xiangkai Sun, Adam L. Shaw, Ran Finkelstein, and Manuel Endres. Benchmarking and fidelity response theory of high-fidelity rydberg entangling gates. *PRX Quantum*, 6:010331, Feb 2025.

[35] J A Muniz, M Stone, D T Stack, M Jaffe, J M Kindem, L Wadleigh, E Zalys-Geller, X Zhang, C-A Chen, M A Norcia, J Epstein, E Halperin, F Hummel, T Wilkason, M Li, K Barnes, P Battaglino, T C Bohdanowicz, G Booth, A Brown, M O Brown, W B Cairncross, K Cassella, R Coxe, D Crow, M Feldkamp, C Griger, A Heinz, A M W Jones, H Kim, J King, K Kotru, J Lauigan, J Marjanovic, E Megidish, M Meredith, M McDonald, R Morshead, S Narayanaswami, C Nishiguchi, T Paule, K A Pawlak, K L Pudenz, D Rodríguez Pérez, A Ryou, J Simon, A Smull, M Urbanek, R J M van de Veerdonk, Z Vendeiro, T-Y Wu, X Xie, and B J Bloom. High-fidelity universal gates in the ^{171}Yb ground state nuclear spin qubit. November 2024.

[36] A. N. Craddock, J. Hannegan, D. P. Ornelas-Huerta, J. D. Siverns, A. J. Hachtel, E. A. Goldschmidt, J. V. Porto, Q. Quraishi, and S. L. Rolston. Quantum interference between photons from an atomic ensemble and a remote atomic ion. *Phys. Rev. Lett.*, 123:213601, Nov 2019.

[37] Or Katz and Ofer Firstenberg. Light storage for one second in room-temperature alkali vapor. *Nat. Commun.*, 9(1), May 2018.

[38] Anindya Rastogi, Erhan Saglamyurek, Taras Hrushevskyi, Scott Hubele, and Lindsay J LeBlanc. Discerning quantum memories based on electromagnetically-induced-transparency and Autler-Townes-splitting protocols. *Phys. Rev. A (Coll. Park.)*, 100(1), July 2019.

[39] Gianni Buser, Roberto Mottola, Björn Cotting, Janik Wolters, and Philipp Treutlein. Single-photon storage in a ground-state vapor cell quantum memory. *PRX Quantum*, 3:020349, Jun 2022.

[40] M. Fleischhauer and M. D. Lukin. Dark-state polaritons in electromagnetically induced transparency. *Phys. Rev. Lett.*, 84:5094–5097, May 2000.

[41] Ran Finkelstein, Samir Bali, Ofer Firstenberg, and Irina Novikova. A practical guide to electromagnetically induced transparency in atomic vapor. *New Journal of Physics*, 25(3):035001, mar 2023.

[42] Omri Davidson, Ohad Yogev, Eilon Poem, and Ofer Firstenberg. Single-photon synchronization with a room-temperature atomic quantum memory. *Phys. Rev. Lett.*, 131:033601, Jul 2023.

[43] David J. Fulton, Sara Shepherd, Richard R. Moseley, Bruce D. Sinclair, and Malcolm H. Dunn. Continuous-wave electromagnetically induced transparency: A comparison of v, Λ, and cascade systems. *Phys. Rev. A*, 52:2302–2311, Sep 1995.

[44] Wolfgang Ketterle. Atomic, molecular, and optical physics lecture notes.

[45] Andrew Zangwill. *Modern Electrodynamics*. Cambridge, 2013.

[46] J Borregaard, M Zugenmaier, J M Petersen, H Shen, G Vasilakis, K Jensen, E S Polzik, and A S Sørensen. Scalable photonic network architecture based on motional averaging in room temperature gas. *Nat. Commun.*, 7(1):11356, April 2016.

[47] Sreraman Muralidharan, Linshu Li, Jungsang Kim, Norbert Lütkenhaus, Mikhail D Lukin, and Liang Jiang. Optimal architectures for long distance quantum communication. *Scientific Reports*, 6(1):20463, February 2016.

[48] Sonali Gera, Chase Wallace, Mael Flament, Alessia Scriminich, Mehdi Namazi, Youngshin Kim, Steven Sagona-Stophel, Giuseppe Vallone, Paolo Villoresi, and Eden Figueroa. Hong-Ou-Mandel interference of single-photon-level pulses stored in independent room-temperature quantum memories. *npj Quantum Information*, 10(1):10, January 2024.

[49] F W Sun and C W Wong. Indistinguishability of independent single photons. *Phys. Rev. A*, 79(1), January 2009.

[50] Leonard Mandel and Emil Wolf. *Optical coherence and quantum optics*. Cambridge University Press, Cambridge, England, April 2013.

[51] Yunfei Wang, Jianfeng Li, Shanchao Zhang, Keyu Su, Yiru Zhou, Kaiyu Liao, Shengwang Du, Hui Yan, and Shi-Liang Zhu. Efficient quantum memory for single-photon polarization qubits. *Nat. Photonics*, 13(5):346–351, May 2019.

[52] E Knill, R Laflamme, and G J Milburn. A scheme for efficient quantum computation with linear optics. *Nature*, 409(6816):46–52, January 2001.

[53] J Appel, P J Windpassinger, D Oblak, U B Hoff, N Kjaergaard, and E S Polzik. Mesoscopic atomic entanglement for precision measurements beyond the standard quantum limit. *Proc. Natl. Acad. Sci. U. S. A.*, 106(27):10960–10965, July 2009.

[54] Mikael Afzelius, Nicolas Gisin, and Hugues de Riedmatten. Quantum memory for photons. *Physics Today*, 68(12):42–47, 12 2015.

[55] Hugues de Riedmatten, Mikael Afzelius, Matthias U Staudt, Christoph Simon, and Nicolas Gisin. A solid-state light-matter interface at the single-photon level. *Nature*, 456(7223):773–777, December 2008.

[56] Mikael Afzelius, Christoph Simon, Hugues de Riedmatten, and Nicolas Gisin. Multimode quantum memory based on atomic frequency combs. *Phys. Rev. A*, 79(5), May 2009.

[57] M Hosseini, B M Sparkes, G Campbell, P K Lam, and B C Buchler. High efficiency coherent optical memory with warm rubidium vapour. *Nat. Commun.*, 2(1):174, February 2011.

[58] Eric Bersin, Madison Sutula, Yan Qi Huan, Aziza Suleymanzade, Daniel R Assumpcao, Yan-Cheng Wei, Pieter-Jan Stas, Can M Knaut, Erik N Knall, Carsten Langrock, Neil Sinclair, Ryan Murphy, Ralf Riedinger, Matthew Yeh, C J Xin, Saumil Bandyopadhyay, Denis D Sukachev, Bartholomeus Machielse, David S Levonian, Mihir K Bhaskar, Scott Hamilton, Hongkun Park, Marko Lončar, Martin M Fejer, P Benjamin Dixon, Dirk R Englund, and Mikhail D Lukin. Telecom networking with a diamond quantum memory. *arXiv [quant-ph]*, 2023.

[59] C M Knaut, A Suleymanzade, Y-C Wei, D R Assumpcao, P-J Stas, Y Q Huan, B Machielse, E N Knall, M Sutula, G Baranes, N Sinclair, C De-Eknamkul, D S Levonian, M K Bhaskar, H Park, M Lončar, and M D Lukin. Entanglement of nanophotonic quantum memory nodes in a telecom network. *Nature*, 629(8012):573–578, May 2024.

[60] Antonio Ortu, Adrian Holzäpfel, Jean Etesse, and Mikael Afzelius. Storage of photonic time-bin qubits for up to 20 ms in a rare-earth doped crystal. *Npj Quantum Inf.*, 8(1), March 2022.

[61] Alexey V Gorshkov, Axel André, Michael Fleischhauer, Anders S Sørensen, and Mikhail D Lukin. Universal approach to optimal photon storage in atomic media. *Phys. Rev. Lett.*, 98(12):123601, March 2007.

[62] Frédéric Grosshans and Philippe Grangier. Quantum cloning and teleportation criteria for continuous quantum variables. *Phys. Rev. A*, 64:010301, Jun 2001.

[63] Lijun Ma, Oliver Slattery, and Xiao Tang. Optical quantum memory based on electromagnetically induced transparency. *J. Opt.*, 19(4):043001, April 2017.

[64] Wenhao Li, Mikhail Balabas, Xiang Peng, Szymon Pustelny, Arne Wickenbrock, Yucheng Yang, Hong Guo, and Dmitry Budker. Investigation of antirelaxation wall coatings beyond melting temperatures. In *2017 Conference on Lasers and Electro-Optics (CLEO)*, pages 1–2, 2017.

[65] J. D. Siverns, X. Li, and Q. Quraishi. Ion–photon entanglement and quantum frequency conversion with trapped ba+ ions. *Appl. Opt.*, 56(3):B222–B230, Jan 2017.

[66] James D Siverns, John Hannegan, and Qudsia Quraishi. Neutral-atom wavelength-compatible 780 nm single photons from a trapped ion via quantum frequency conversion. *Phys. Rev. Appl.*, 11(1), January 2019.

[67] John Hannegan, James D Siverns, and Qudsia Quraishi. Entanglement between a trapped-ion qubit and a 780-nm photon via quantum frequency conversion. *Phys. Rev. A (Coll. Park.)*, 106(4), October 2022.

[68] Tim van Leent, Matthias Bock, Florian Fertig, Robert Garthoff, Sebastian Eppelt, Yiru Zhou, Pooja Malik, Matthias Seubert, Tobias Bauer, Wenjamin Rosenfeld, Wei Zhang, Christoph Becher, and Harald Weinfurter. Entangling single atoms over 33 km telecom fibre. *Nature*, 607(7917):69–73, July 2022.

[69] D P Ornelas-Huerta, A N Craddock, E A Goldschmidt, A J Hachtel, Y Wang, P Bienias, A V Gorshkov, S L Rolston, and J V Porto. On-demand indistinguishable single photons from an efficient and pure source based on a rydberg ensemble. *Optica*, 7(7):813, July 2020.

[70] R. Paschotta. Acousto-optic modulators. RP Photonics Encyclopedia. Available online at `https://www.rp-photonics.com/acousto_optic_modulators.html`.

[71] D. J. McCarron. A guide to acousto-optic modulators. Bender Group at Jila Webpage, December 2007.